'Gobbling drops': the jetting–dripping transition in flows of polymer solutions

C. CLASEN[1]†, J. BICO[2], V. M. ENTOV[3] AND G. H. McKINLEY[4]

[1]Departement Chemische Ingenieurstechnieken, Katholieke Universiteit Leuven, 3001 Leuven, Belgium

[2]Physique et Mécanique des Milieux Hétérogènes (PMMH), CNRS UMR7636, ESPCI-ParisTech, Univ. Paris 6, Univ. Paris 7, 75005 Paris, France

[3]Institute for Problems in Mechanics, Russian Academy of Sciences, Moscow, 119526 Russia

[4]Hatsopoulos Microfluids Laboratory, Department of Mechanical Engineering, Massachusetts Institute of Technology, Cambridge, MA 02139, USA

This paper discusses the breakup of capillary jets of dilute polymer solutions and the dynamics associated with the transition from dripping to jetting. High-speed digital video imaging reveals a new scenario of transition and breakup via periodic growth and detachment of large terminal drops. The underlying mechanism is discussed and a basic theory for the mechanism of breakup is also presented. The dynamics of the terminal drop growth and trajectory prove to be governed primarily by mass and momentum balances involving capillary, gravity and inertial forces, whilst the drop detachment event is controlled by the kinetics of the thinning process in the viscoelastic ligaments that connect the drops. This thinning process of the ligaments that are subjected to a constant axial force is driven by surface tension and resisted by the viscoelasticity of the dissolved polymeric molecules. Analysis of this transition provides a new experimental method to probe the rheological properties of solutions when minute concentrations of macromolecules have been added.

---

1. Gobbling: introduction and physical picture

A peculiar and apparently new pattern of breakup has been observed in experiments with jets of dilute polymer solutions at flow rates close to the critical rates corresponding to a transition from dripping to jetting flow. In this regime, a thin and slender jet terminates with a large terminal drop that is of much greater radius than either the nozzle or the drops usually observed in the course of normal capillary breakup of a Newtonian fluid jet. A representative sequence of digital images is shown in figure 1. Although the jet is apparently in a steady-state, the terminal drop experiences periodic dynamics. The drop first grows while slowly moving upstream, the direction of motion eventually reverses, the drop then accelerates, becomes much wider than the incoming jet, and eventually detaches. A new terminal drop then forms and the process repeats itself.

As a result of capillary instabilities, the primary jet starts to develop the beads-on-string pattern characteristic of polymeric jets (Goldin *et al.* 1969; Entov & Yarin 1984; Bousfield *et al.* 1986; Bazilevskii *et al.* 1990*b*) before merging with the terminal drop. Therefore, the process resembles the 'gobbling' ('to gobble – to swallow greedily

---

† Email address for correspondence: christian.clasen@cit.kuleuven.be
(This paper is dedicated to the memory of Vladimir M. Entov (1937–2008))

FIGURE 1. The 'gobbling' phenomenon: a large terminal drop periodically develops at the end of a thin jet of a viscoelastic fluid (100 ppm PAA solution, $Q = 39.7\,\mathrm{mm^3\,s^{-1}}$, $R_i = 0.125\,\mathrm{mm}$). A sequence of video images is shown; the time interval between consecutive images is 6 ms.

or hastily in large pieces; gulp': American College Standard Reference Dictionary) of a chain of tiny beads by a greedy terminal drop, until it is 'sated' or 'saturated' and falls off. In some cases, the terminal drop can 'swallow' up to several scores of beads before detachment. A movie of the gobbling phenomenon can be found at http://web.mit.edu/clasen/Public/gobbling.avi.

The 'gobbling' phenomenon is specific to macromolecular solutions and is never observed in experiments with jets of pure water or other Newtonian fluids. However, even minute amounts of polymeric additive bring it into existence. If one focuses on the central axial column, it is clear that the primary role of the polymeric additive is to stabilize the later stages of the capillary thinning process and severely retard the inertial breakup of the fluid column (Christanti & Walker 2001; Amarouchene *et al.* 2001; Tirtaatmadja, McKinley & Cooper-White 2006). This stabilization then enables us to image the temporal evolution and axial development of a beads-on-a-string morphology along the jet. Somewhat analogous bead dynamics can be seen even with Newtonian fluids when a thin annular film of viscous fluid is coated on a solid fibre (as described originally by Boys 1912 and studied in detail by Kliakhandler, Davis & Bankoff 2001; Craster, Matar & Papageorgiou 2005 and references therein). In the present case the rigid central fibre is replaced by the highly elongated polymer molecules in the thin viscoelastic ligaments connecting the drops .

The dramatic effects of dilute amounts of high-molecular-weight additives on the breakup of aqueous fluid filaments is well known and has been extensively studied since the pioneering work of Middleman (1965) and Goldin *et al.* (1969). The hydrodynamic consequences of small amounts of polymeric additives can be rationalized in terms of the unravelling and extension of the initially coiled polymeric molecules by strong extensional flows (Entov & Yarin 1984; Bazilevskii *et al.* 1990b; Anna & McKinley 2001; Clasen *et al.* 2006b). In the case of steady jets issuing from a nozzle at high flow rates, significant elastic stresses can be generated (even for dilute polymer solutions) which affect the breakup length of the jet and the ensuing droplet size distribution (Bousfield *et al.* 1986; Christanti & Walker 2001). In the case of dripping from a faucet at very low flow rates, the presence of even dilute concentrations of polymer can dramatically extend the time to pinch off and inhibit the existence of satellite droplets (Amarouchene *et al.* 2001; Tirtaatmadja *et al.* 2006; Sattler, Wagner & Eggers 2008). In each case, the large elongational viscosity of the

highly stretched macromolecules results in a change in the local dominant balance of forces in the local necking region (see McKinley 2005 for a recent review). What has been much less studied is the role of a polymeric additive at the critical flow rates close to the jetting–dripping transition. Even in a Newtonian fluid this transition can exhibit complex or chaotic dynamics (see, for example, Ambravaneswaran *et al.* 2004; Coullet, Mahadevan & Riera 2005; Sauter & Buggisch 2005) and recent simulations with an inelastic generalized Newtonian fluid (Yildirim & Basaran 2006) show that these dynamics may be substantially modified by the incorporation of nonlinear fluid rheology. In the present work we investigate the role of fluid elasticity and a finite polymeric relaxation time on the dynamics observed at the dripping–jetting transition which result in the gobbling drop effect. A recent study by Clanet & Lasheras (1999) provides the necessary background information on the dripping–jetting transition in water and also introduces many of the essential elements for the dynamic theory developed below to explain the gobbling phenomenon.

The paper is organized as follows. In §2 we describe the experimental observations and qualitative characteristics of the gobbling phenomenon. In §3, an elementary dynamic theory of gobbling is presented, based on the assumption that gobbling is governed by mass and momentum transfer from a jet moving at constant velocity to a terminal drop in a gravitational free fall. This model introduces a breakup time for the jet as an adjustable parameter and we also delimit the range of other physical parameters for which gobbling is observed. In §4, the observed dependence of the breakup time on the jet radius is finally explained quantitatively as a process governed by a forced thinning of the interconnecting polymeric fluid ligament under the combined action of the lateral capillary pressure and an axial force.

2. Experiments

2.1. *Fluid properties*

Experiments were performed with several dilute aqueous polymer solutions, and compared with benchmark experiments performed using pure water. The main body of results reported below relates to experiments with a 100 ppm solution of polyacrylamide (PAA) in water. The polymer solution was prepared by dissolving 0.01 wt % linear polyacrylamide (Praestol 2540, Stockhausen) in deionized water. The fluid was gently shaken for 5 days to ensure homogeneous mixing. The polymer molecular mass was determined by intrinsic viscometry to be $M_w = 7.5 \times 10^6 \, \mathrm{g \, mol^{-1}}$ which corresponds to a degree of polymerization of $P \sim 10^5$. The molecular extensibility of the chains depends on the ratio of the fully extended chain length ($\sim P$) to the r.m.s. size of the random coil under equilibrium conditions ($\sim P^{1/2}$). Estimates of the critical overlap concentration c^* based on this degree of polymerization give $c^* = 0.0182 \, \mathrm{wt \,\%}$. Thus, we are dealing with a dilute ($c < c^*$) solution of a flexible long-chain polymer capable of developing significant elastic stretch ($\sim P^{1/2}$) in strong extensional flows.

The zero shear rate viscosity for this solution was determined with a capillary viscometer to be $\eta_0 = 2.74 \, \mathrm{mPa.s}$. The surface tension of the tested solution was determined using a Wilhelmy plate type tensiometer (Krüss K-10) to be $\gamma = 61.4 \, \mathrm{mN \, m^{-1}}$.

High-molecular-mass polymer solutions are prone to develop thin liquid filaments, such as those seen between the beads in figure 1. This enables the determination of a longest relaxation time λ for the solution from the direct observation of the capillary thinning kinetics of thin liquid filaments, as discussed in Bazilevskii, Entov
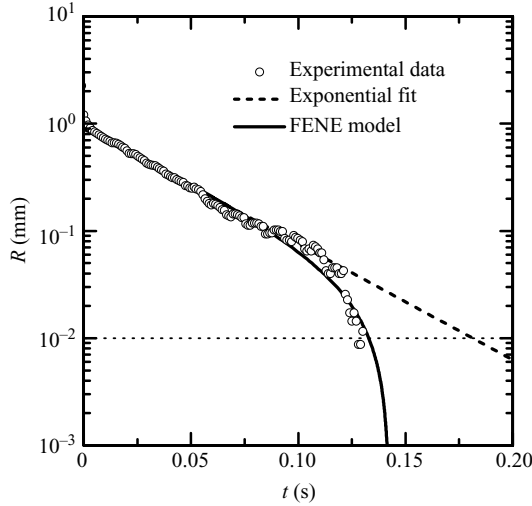
FIGURE 2. Kinetics of the capillary thinning of a liquid filament of aqueous polyacrylamide solution (100 ppm) in a CABER-1 capillary breakup rheometer showing the filament radius versus time. Raw data (points), approximation by an exponential dependence (broken line) and by a finitely extensible nonlinear elastic dumbbell (FENE) model (solid line). The limit of the optical resolution (10 μm) is shown by the dotted line.

& Rozhkov (1990*a*, 2001); Entov & Hinch (1997); McKinley & Tripathi (2000); Anna & McKinley (2001) and Clasen *et al.* (2006*b*). The experiments were carried out using an extensional rheometer (CABER-1, Cambridge Polymer Group) described in Braithwaite & Spiegelberg (2001).

In these experiments, the radius of the thinning filament is monitored by a laser micrometre, and the time dependence of the radius R is fitted with the exponential expression:

$$R(t) \sim \exp(-t/\theta)$$

that is valid at intermediate times for flexible polymer chains that have not been fully extended. Eventually, the filament breaks in finite time once the finite extensibility limit of the polymer chains is reached.

According to the theory presented elsewhere (Bazilevskii *et al.* 1990*a*; Entov & Hinch 1997; Anna & McKinley 2001; Bazilevskii *et al.* 2001; Plog, Kulicke & Clasen 2005 and Clasen *et al.* 2006*a*), the longest relaxation time can then be evaluated as:

$$\lambda = \tfrac{1}{3}\theta.$$

From the exponential decay regime of the experimental capillary thinning data in figure 2 we find $\lambda \approx 0.012$ s.

2.2. *From jetting to dripping*

Thin jets of fluid were expelled vertically downwards from standard syringe tips of different diameters; the tip inner radius range was 0.05–0.76 mm. Experiments were performed at several different controlled flow rates using a precision syringe pump (Harvard Apparatus PhD 2000).

Starting from initial conditions of a steady jet, a number of different flow regimes are successively observed as the flow rate of the polymer solutions is progressively decreased. In particular, the gobbling phenomenon is observed only within a certain
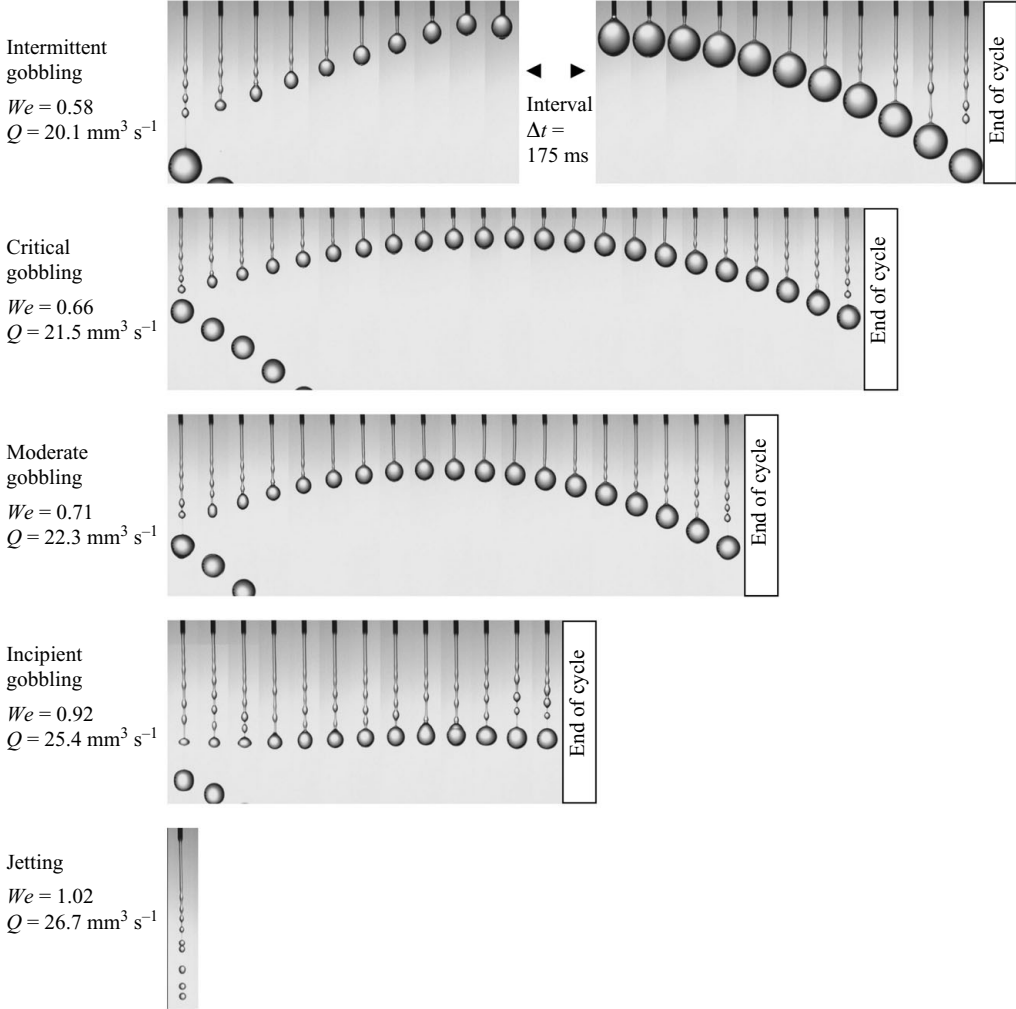
FIGURE 3. Characteristic stages of gobbling with a nozzle of radius $R_i = 0.075$ mm as the flow rate is progressively decreased from 26.7 mm^3 s^{-1} to 20.1 mm^3 s^{-1} (from the bottom to top sequence of images). Images are recorded at 2000 fps, the interval between 2 consecutive shown frames is $\Delta t = 5$ ms.

range of flow rates. In figure 3 we show visualizations of the characteristic stages of the gobbling phenomenon for a nozzle with an inner diameter of $R_i = 0.075$ mm and flow rates Q ranging from 20.1 to 26.7 mm^3 s^{-1}. Starting from a high flow rate, a continuous jet flow is observed. Due to the classical Rayleigh–Plateau instability, the jet rapidly breaks into drops with a characteristic size that is of the order of the diameter of the jet. As the flow rate is lowered, the terminal drop begins to 'gobble' the jet. At this 'incipient gobbling' stage, the terminal drop grows but remains nearly stationary before detaching. Upon decreasing the flow rate further, we observe the onset of a parabolic trajectory of the terminal drop, resulting in excursions of increasing amplitude in the length of the jet. Passing through the stages of 'moderate' gobbling (where the amplitude is half the maximum length of the jet), we finally reach 'critical' gobbling when the gobbling amplitude reaches the maximum length of

the jet and the terminal drop almost reconnects to the nozzle. Any further decrease in the flow rate results in a reconnection of the terminal drop to the nozzle and a longer interval during which the terminal drop stays connected to the nozzle before detaching. We refer to this regime as 'intermittent gobbling' rather than a form of dripping because the large terminal drop still 'gobbles' up smaller beads as it separates and slowly accelerates downwards under gravity. A dripping transition is reached once the flow rate is low enough to allow single drops to detach from the nozzle without the generation of additional smaller beads during the detachment process. The periodic growth of the jet length and drop size occurs over a narrow range of flow rates, which makes the phenomenon rather sensitive to specific experimental conditions that parameterize the critical flow rate, especially the polymer concentration and solution 'freshness'. Thus, an appreciable shift in critical values may be observed between different series of experiments carried out with different batches of solution of the same nominal polymer concentration.

In an effort to quantify this time-dependent phenomenon, an experimental technique has been developed based on frame-by-frame computer-aided analysis of successive video images produced by a digital high-speed camera (Clasen *et al.* 2004). Details of this technique are outlined below.

2.3. *Detailed analysis of 'gobbling': data processing technique*

Images of the gobbling jet were captured with a high speed camera (Phantom 5, Vision Research Inc.) working at a frame rate of 2000 fps and with an image size of 256×1024 square pixel. A macro objective (Canon 70 F/2.8) gives a spatial resolution of $25\,\mu\text{m pixel}^{-1}$.

Frame by frame analysis of these images reveals many important features of the gobbling phenomenon. The starting point of the analysis is the conversion of the digital images produced by the camera into profiles of the free surface of the jet, i.e. the radius versus distance from the nozzle tip $R(z)$ at a given time. An image analysis code was specifically developed for this purpose using LabView (National Instruments). In particular, critical features of the evolving jet can be extracted, such as the location of the terminal drop or the position of asperities on the continuous part of the jet that evolve in time into well-defined beads. Since capillary instability waves do not move relative to the fluid in the jet (Rayleigh 1879, 1892; Weber 1931; Eggers 1997), the positions of these asperities can be used as markers to directly measure the velocity distribution along the jet. The position $L(t)$ of the centre of the terminal drop, as well as the position of the individual beads $X(t)$ can be extracted as demonstrated in figures 4(*a*) and 4(*b*) to construct 'XLt diagrams' (figure 4*c*). Subsequent processing of the free surface profiles allows the determination of the terminal drop volume $\mathscr{V}$, as well as the radius and position of the thin ligaments connecting the beads. The fragment of an XLt diagram shown in figure 4(*c*) is typical for a well-developed 'gobbling' regime. It clearly illustrates an important feature of gobbling in thin jets: the fluid velocity is, to a first approximation, constant along the jet. Indeed, thin solid lines in these space–time diagrams are essentially parallel to the traces of the beads. They have a constant slope corresponding to the jet velocity (in this particular case of $U_0 = 0.5\,\text{m s}^{-1}$) which remains fairly constant during the cycle. In thicker jets the acceleration caused by gravity becomes important, and the trajectories of the individual beads in XLt diagrams tend to become parabolic. Although the terminal drop moves slowly upwards and downwards prior to detachment, the primary jet remains unaffected by this oscillation. This is a characteristic of convective jet flows, in which fluid particles move purely by their own inertia. This observation is confirmed
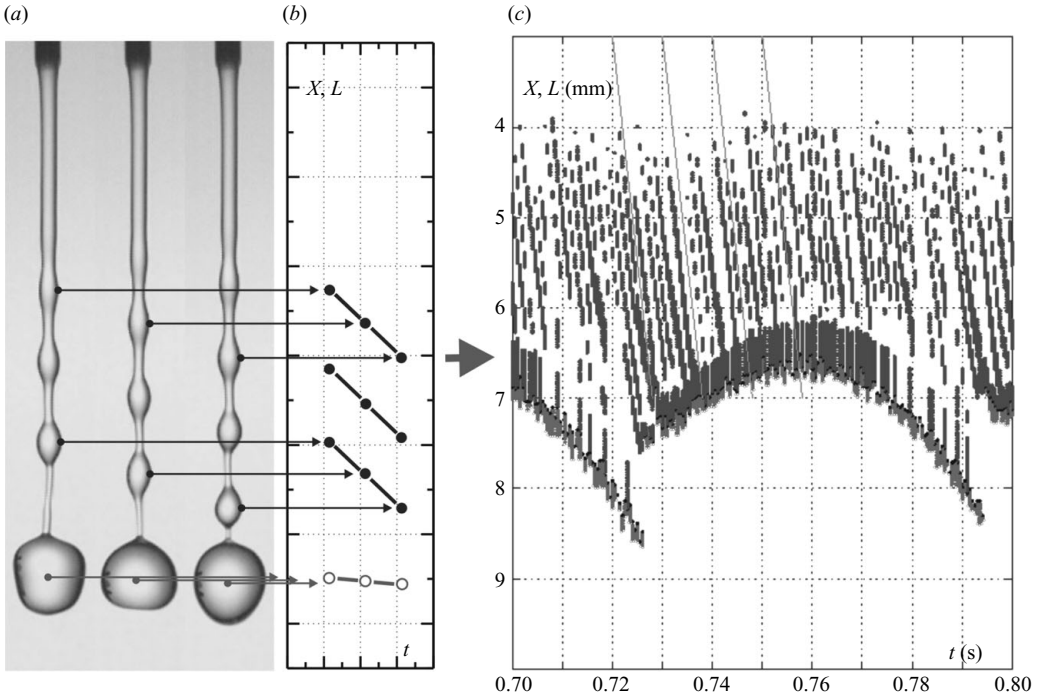
FIGURE 4. (*a*)–(*b*) Construction of an XLt diagram. Traces of the terminal drop position $L(t)$ (hollow circles) and individual asperity locations $X(t)$ on the falling jet (filled points) are displayed in three video frames each separated by $\delta t = 1$ ms. (*c*) Example of an XLt diagram for a jet issuing from a nozzle of $R_i = 0.075$ mm at a flow rate of 22.3 mm^3 s^{-1}. Thin solid lines of constant slope are essentially parallel to the bead traces indicating that the beads move with constant velocity until they merge with the terminal drop, which is following a periodic trajectory. Such a flow pattern is typical of the fully developed 'gobbling' regime observed for thin viscoelastic jets.

by scrutinizing other similar XLt diagrams for thin jets of polymer solutions (not reproduced here) and serves as a basis of the elementary dynamical model which is presented in §3.3.

The direct measurement of the jet velocity can also be used to confirm the initial radius R_0 of the jet. Due to the combined action of capillary and inertia forces in the vicinity of the nozzle tip, the radius of the issuing jet differs significantly from both the internal nozzle tip radius R_i and external nozzle tip radius R_e (Clanet & Lasheras 1999). In principle, the jet radius R_0 could be determined directly from the digitized jet profiles. However, due to the slenderness of the jet the radius corresponds to only a few pixels, leading to significant imprecision (e.g. in figure 3 the jet radius is $R_0 \approx 90\,\mu$m $\cong 3.6$ pixel).

A more reliable way to determine the initial jet radius R_0 is to use the relation

$$Q = \pi R_0^2 U_0. \qquad (2.1)$$

As the flow rate Q is accurately controlled by the syringe pump, and the jet velocity U_0 is directly measured by the marker traces, R_0 is readily evaluated. The observed jet radius R_0 can then be related to the nozzle inner radius R_i. The results are presented in figure 5. The data points are well described by a linear relation
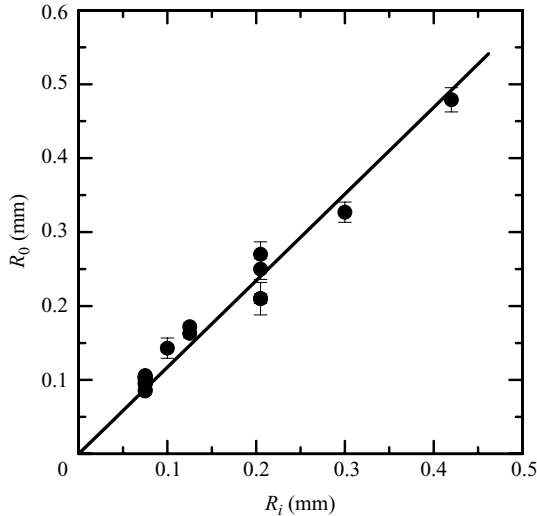
$$R_0 = 1.17\, R_i, \qquad (2.2)$$

FIGURE 5. Measured jet radius R_0 as a function of the nozzle inner radius R_i: experimental data for PAA solutions (●) and linear fit $R_0 = 1.17\ R_i$ (straight line).

with a correlation coefficient $r^2 = 0.985$. This relationship is employed systematically in later developments.

3. Theoretical analysis

3.1. *The dripping and jetting transitions (following Clanet and Lasheras)*

The transition from dripping to jetting has been investigated in detail in the past for the case of a low viscous Newtonian liquid (water in most situations). In particular, Clanet & Lasheras (1999) give a precise definition and a comprehensive description of the different flow transitions observed when increasing the flow rate of a Newtonian liquid exiting a thin nozzle.

A first 'dripping' transition characterizes the transition from a time-regular drop formation with constant drop volumes ('periodic dripping') to a quasi-periodic or chaotic behaviour ('dripping faucet') during which the mass of the detaching drops vary from one to the next.

A second 'jetting' transition occurs when the detachment point of drops suddenly moves downstream, away from the nozzle. As the flow rate is progressively increased, longer jets are observed. The authors precisely quantified this loose definition of a jetting transition by measuring the length of the jet. They defined the transition as the flow rate required to obtain a jet ten times longer than its diameter (changing this arbitrarily chosen aspect ratio, does not modify significantly the critical flow rate).

In the absence of gravitational effects, the criterion for the transition is straightforward: the momentum flux of the liquid has to balance or exceed upstream capillary forces originating from newly created surface at the nozzle. If U_0 is the velocity of the fluid exiting the nozzle, R_i the inner radius of the nozzle, γ and ρ the respective surface tension and density of the liquid, the transition is expected when $\rho U_0^2 R_i^2 \gtrsim \gamma R_i$, i.e. $We \gtrsim 1$, where We refers to the Weber number, $We = \rho U_0^2 R_i / \gamma$.

The case of finite gravity is more complex since the weight of the drop plays an important role in its detachment from the tip. In this case Clanet & Lasheras (1999)
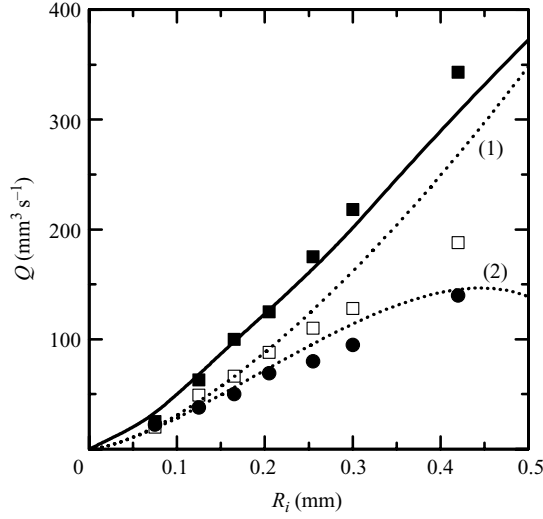
FIGURE 6. Critical flow rates versus nozzle inner radius for water and an aqueous solution of 100 ppm PAA. Open squares: dripping transition for water; closed squares: jetting transition for water; closed circles: jetting transition for the PAA solution; solid line: prediction of jetting transition for water according to formula (3.1) developed by Clanet & Lasheras (1999); dotted line (1): critical flow rate Q_{cr0} from (3.9); dotted line (2): critical flow rate in the presence of gravity Q_{cr} from (3.10).

formulated the critical Weber number at the jetting transition as

$$We_c = 2\sqrt{\frac{Bo_e}{Bo}}\left[S - (S^2 - 1)^{1/2}\right]^2; \quad S = 1 + 2K(Bo_e Bo)^{1/2}, \tag{3.1}$$

with

$$We = \frac{\rho U_0^2 R_i}{\gamma}, \quad Bo = \frac{\rho g R_i^2}{\gamma}, \quad Bo_e = \frac{\rho g R_e^2}{\gamma}. \tag{3.2}$$

The Bond numbers Bo and Bo_e compare capillary forces to gravity and are evaluated using the inner tip radius R_i and the outer radius R_e, respectively; K is a numerical constant equal to 0.37 in the case of water jets in air. As intuition would suggest, increasing the importance of gravity results in lower critical Weber numbers.

We measured experimentally the dripping and jetting transitions for water and a dilute polymer solution (100 ppm polyacrylamide solution). The results are shown in figure 6 and compared with the expression from Clanet and Lasheras given by (3.1). Obviously, the data for water are in good agreement with the theoretical prediction for a jetting transition. Conversely, the critical flow rates obtained with the polymer solution at the jetting transition are much smaller than the corresponding values for water.

Furthermore, when trying to reach the dripping transition for the polymer solution by further lowering the flow rates, the novel gobbling regime is observed. The length of the jet is approximately constant only for higher flow rates close to the jetting transition (the case of 'incipient' gobbling described in figure 3). As the flow rate is lowered further the jet undergoes subsequently the different stages of gobbling described in figure 3. Although initially developed for low viscous Newtonian liquids, we re-explore in the following sections the model from Clanet and Lasheras with a
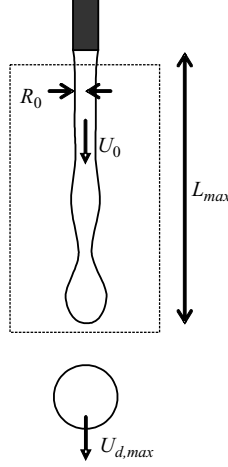
FIGURE 7. Steady jet issuing from a nozzle. The dashed box delimits the control volume for the mass and momentum balance.

slightly different presentation that takes into account the peculiar additional features of dilute polymeric solutions (persistent liquid filaments and rheological stresses).

3.2. *A jetting transition depending on a positive momentum flux*

The experimental observation of nearly constant jet lengths at the jetting transition suggests a simplified description of the problem as sketched in figure 7. We consider a steady jet issuing from a nozzle downwards along the z-axis and eventually breaking at a distance L_{max} from the nozzle. We choose a control volume bounded by two horizontal cross-sections, one within the contiguous part of the jet close to the nozzle, and the other one just after the jet breaking point.

The time-averaged momentum balance for this control volume integrated over one period reads

$$-F + \pi \rho R_0^2 U_0^2 + \mathscr{V}_j \rho g = \frac{\rho \mathscr{V}_{max} U_{d,max}}{T}, \qquad (3.3)$$

where F is the tensile force at the upstream cross-section, R_0 the jet radius, U_0 the jet velocity, $\mathscr{V}_j$ the time-averaged fluid volume between the two cross-sections, T the period between two detaching drops passing through the lower cross-section, $\mathscr{V}_{max}$ the volume of each of these detaching drops and $U_{d,max}$ their velocity.

The net tensile force F supporting the jet consists of two parts:

$$F = 2\pi R_0 \gamma + \pi R_0^2 \tau_{zz}, \qquad (3.4)$$

where the first part takes into account the surface tension of the newly created surface at the upper cross-section of the control volume while τ_{zz} refers to other axial stresses in the jet. These axial stresses in the slender jet can be expressed in terms of two contributions $\tau_{zz} \equiv \sigma_{zz} - p$, where the pressure p can be replaced by the radial stress balance $p = \gamma/R_0 + \sigma_{rr}$:

$$\tau_{zz} = (\sigma_{zz} - \sigma_{rr}) - \frac{\gamma}{R_0}. \qquad (3.5)$$

Here, the second term on the right-hand side represents the capillary pressure at the lateral surface of the jet, while the first term is the 'rheological stress' contribution $\sigma_{rheol} \equiv (\sigma_{zz} - \sigma_{rr})$ resulting from the deformation of the viscoelastic fluid (i.e. a normal

stress difference). Combining with (3.4) we obtain

$$F = \pi R_0 \gamma + \pi R_0^2 \sigma_{rheol}. \tag{3.6}$$

The solution experiences a strong shear rate in the syringe needle ($\dot{\gamma} \sim 10^5$ s^{-1} for the typical conditions of our experiments) during a residence time of the same order of the relaxation time of the low concentrated polymer molecules ($L_{needle}/U_0 \sim 20$ ms). Nevertheless, we neglect the initial elastic strain of the dilute polymers in the uniform jet considered in this simplified model. In this condition, the 'rheological stress' σ_{rheol} is negligible, which leads to

$$F = \pi R_0 \gamma. \tag{3.7}$$

This formulation differs from Clanet and Lasheras by a factor of 2, but is in agreement with the expression that Griffith used when he successfully measured the surface tension of glass (Griffith 1926). This factor of 2 has apparently lead to some controversy as discussed in Eggers (1997), who also gives an expression equivalent to (3.7).

With this new expression for the tensile force, the momentum balance (3.3) becomes

$$-\pi R_0 \gamma + \pi \rho R_0^2 U_0^2 + \mathcal{V}_j \rho g = \frac{\rho \mathcal{V}_{max} U_{d,max}}{T}. \tag{3.8}$$

Since the right-hand side of (3.8) must be positive, it implies a lower bound Q_{cr} for the jet flow rate $Q = \pi R_0^2 U_0$:

$$Q \geqslant Q_{cr} = Q_{cr0} \left(1 - \frac{\mathcal{V}_j \rho g}{\pi R_0 \gamma} \right)^{1/2}, \quad \text{with} \quad Q_{cr0} = \pi R_0^{3/2} \sqrt{\frac{\gamma}{\rho}}, \tag{3.9}$$

where Q_{cr0} is the critical flow rate in the absence of gravity and corresponds to a critical Weber number $We_{cr0} = 1$. This critical flow rate is already considerably lower than the experimentally measured values for pure water as depicted in figure 6. In physical terms, the inequality (3.9) states that the momentum influx *into* the control volume should be sufficient to support a positive momentum flux *out* of the control volume. Taking into account gravitational forces, in particular, if we let $\mathcal{V}_j = \pi R_0^2 L_{max}$, which is appropriate for an uniform jet of length L_{max}, we get

$$Q_{cr} = Q_{cr0} \left(1 - \frac{\rho g R_0 L_{max}}{\gamma} \right)^{1/2}. \tag{3.10}$$

If we first set a higher value of the flow rate, and then begin to slowly decrease it, the continuous jetting regime should not persist later than the point where the flow rate falls below the critical value Q_{cr}. Using experimentally observed values for L_{max} we obtain values close to the critical flow rates observed experimentally for the polymer solutions as shown in figure 6.

It is essential to note that this lower bound on the flow rate in the jet can only be explored experimentally for sufficiently long jet breakup times. This is usually not the case for low viscosity Newtonian liquids and this prevented Clanet and Lasheras from also exploring this boundary and observing the gobbling phenomenon. However, adding a tiny mass fraction of high-molecular-weight polymeric molecules to the solution extends the breakup time and may allow a subsequent exploration of this breakup process.

Although the description above remains qualitative, it introduces the essential ingredients driving the gobbling phenomenon: incoming momentum flux, capillary forces and gravity. We therefore re-explore in the following section a simplified
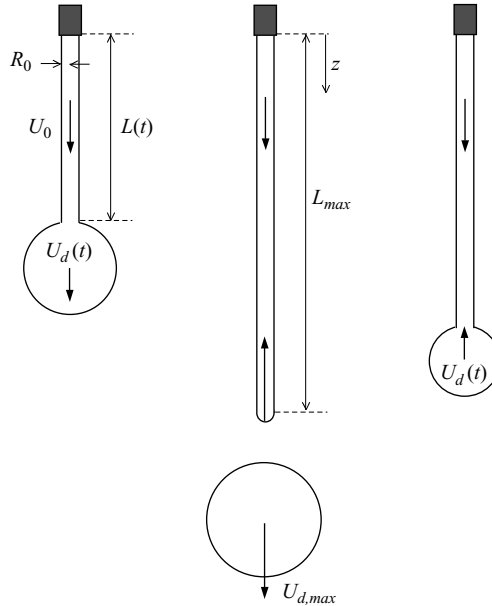
FIGURE 8. Simplified version of the gobbling scenario: the terminal drop is attached to a jet of radius R_0 that is flowing with a uniform velocity U_0. The drop is submitted to its own weight, to the capillary tensile force from the jet and absorbs a momentum flux from the jet. For a critical length L_{max}, the drop detaches from the jet and the same scenario starts again.

dynamic model previously introduced by Clanet and Lasheras which allows for a precise description of the different gobbling stages illustrated in figure 3. We then reconsider the importance of the rheological stress term σ_{rheol} of (3.6) in §4.

3.3. *Elementary dynamical model of gobbling*

Our experimental observations indicate that the gobbling phenomenon results from the interaction between two distinct entities: a steady-state slender jet, and a spherical terminal drop that slowly grows and translates axially. Furthermore, the evolution of the terminal drop does not affect the flow in the jet. This jet is characterized by its initial radius (R_0) and its velocity (U_0) and is independent of the downstream conditions. Indeed, the jet velocity remains nearly constant during the whole cycle as observed in figure 4(c). This property of negligible upstream perturbation is a generic property of convective jetting flows, in contrast to 'pseudo-jet' flows, which are dominated by the upstream transfer of the tension force along the jet. Examples of the latter include fibre spinning (Pearson 1985), coiling of viscous jets (Ribe *et al.* 2006) or slow periodic dripping (Coullet *et al.* 2005). In the following we consider a liquid drop attached to a jet of uniform radius R_0 and uniform velocity U_0 (we incorporate in Appendix B the effects of gravitational acceleration and a slow axial variation in the radius of the jet). As proposed in Clanet & Lasheras (1999), we shall apply principles of mass and momentum conservation to the drop. In addition, we assume that the length of the jet is limited: if the dynamics of the system lead the jet to reach a critical length L_{max}, the drop detaches from the jet and a new terminal drop forms (figure 8). From a more physical point of view, this is equivalent to assuming that the jet breaks in a finite time t_{br}, such that $L_{max} = t_{br}U_0$. In the case of a Newtonian jet of water described by Clanet and Lasheras, this breakup time was governed by a balance between capillarity and inertia $t_{br} \sim (\rho R_0^3/\gamma)^{1/2}$, leading

to rather short lengths L_{max}. With polymer solutions t_{br} can be much larger due to the extensibility of the macromolecules (Anna & McKinley 2001; Wagner *et al.* 2005; Tirtaatmadja *et al.* 2006), which allows for longer jets. In §4 we shall describe in more details how this breakup time t_{br} is connected to the non-Newtonian rheological properties of the fluid in the case of dilute polymer solutions.

The mass balance for the terminal drop is determined by the net mass influx, which depends on the jet flow rate Q, and on the velocity U_d of the terminal drop relative to the jet velocity U_0:

$$\frac{d\mathscr{V}}{dt} = Q \left(1 - \frac{U_d}{U_0} \right), \tag{3.11}$$

where $\mathscr{V}$ is the volume of the growing terminal drop. This net mass influx also enters the linear momentum balance for the terminal drop, together with the tensile force F acting in the jet and the gravitational acceleration:

$$\frac{\rho d(\mathscr{V} U_d)}{dt} = \rho Q \left(U_0 - U_d \right) + \rho \mathscr{V} g - F. \tag{3.12}$$

Clanet and Lasheras have derived an exact parabolic solutions of (3.11) and (3.12) for the terminal drop velocity $U_d(t)$ and position $L(t)$:

$$U_d(t) = U_0 - U^* + \tfrac{1}{3}gt, \qquad L(t) = L_{max} + \left(U_0 - U^* \right) t + \tfrac{1}{6}gt^2, \tag{3.13}$$

with

$$U^* = \sqrt{\frac{F}{\pi \rho R_0^2}}. \tag{3.14}$$

Using the expression for the net tensile force from (3.7), we obtain

$$U^* = \sqrt{\frac{\gamma}{\rho R_0}}. \tag{3.15}$$

In physical terms, U^* represents the velocity of capillary waves propagating along the jet as described by Rayleigh (1879). The integration of the volume conservation (3.11) then gives

$$\mathscr{V}(t) = \pi R_0^2 \left(U^* t - \tfrac{1}{6}gt^2 \right). \tag{3.16}$$

With the selected initial condition, the length of the jet has a maximum value at $t = 0$, which corresponds to the critical jet breakup length L_{max} when the terminal drop has just pinched off. The jet length then initially decreases because the capillary velocity U^* pulling the terminal drop upwards exceeds the incoming axial velocity U_0. As the terminal drop grows and increases its weight, the upward motion eventually ceases and the drop trajectory reverses due to the downward effect of gravitational acceleration. The jet length finally reaches L_{max}, the drop then detaches and the same scenario starts again. We show in Appendix A that even if the initial volume of the drop is finite, the solution eventually converges to the present solution.

Expressions (3.13) and (3.16) allow for a direct comparison with experimental data. Such a comparison is shown in figure 9 for the case illustrated in figure 1 (note that Clanet and Lasheras could not make this comparison with pure water because of short breakup times and, as a consequence, very short jet lengths). The experimental data are described qualitatively by this elementary theory (dashed line). However, the initial upwards slope of the analytical solution corresponding to the recoil velocity dL/dt is steeper than observed in experimental data. The observed trajectories are also slightly asymmetric in comparison with the predicted parabolas. However, these
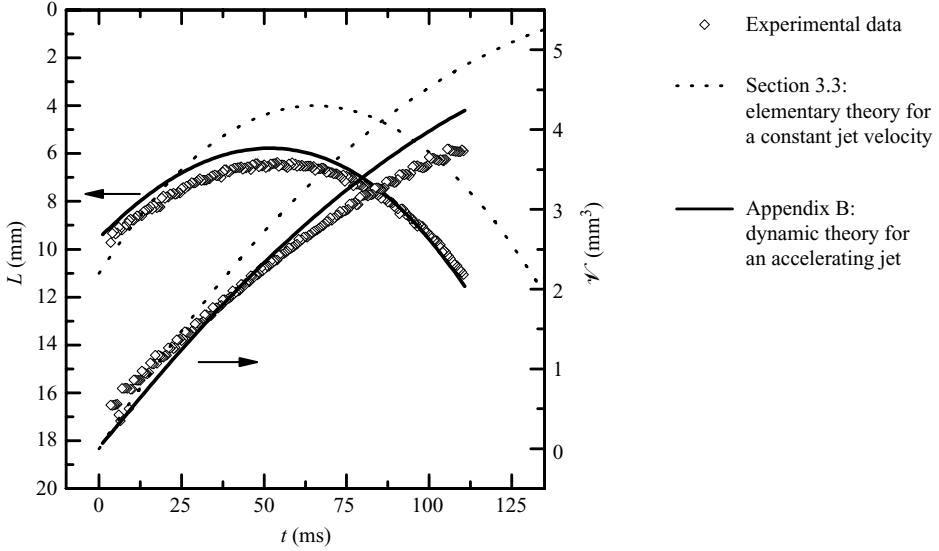
FIGURE 9. Terminal drop position and volume variation during an individual 'gobbling cycle' and their comparison to theory. Nozzle inner radius $R_i = 0.125$ mm, initial jet radius $R_0 = 0.188$ mm, flow rate $Q = 39.7$ mm^3 s^{-1}. Open symbols: experimental data from image processing of the video data; dashed lines: theoretical analytic solution of the elementary theory from equations (3.13) and (3.16); continuous lines: numerical solution of the dynamic theory of Appendix B.

features can be captured by a dynamic theory such as that presented in Appendix B that takes into account the additional acceleration of the fluid in the jet due to gravity. Indeed, the relative contribution of gravity into the momentum balance for the contiguous part of the jet is on the order of the inverse of the Froude Number $\sim g L_{max}/U_0^2$, which ranges from 0.15 to 3.5 for our experiments and can therefore be important (e.g. in the experiment presented in figure 9 this ratio is approximately 0.2).

The dynamic theory described in Appendix B is capable of describing the gobbling dynamics quantitatively as can be seen in figure 9. It also provides a more accurate description of the breakup time: because the liquid accelerates, the actual 'time of flight' of a fluid particle exiting from the nozzle is smaller than $t_{br} = L_{max}/U_0$. However, the dynamic model contains the same simple mass and momentum balances introduced in the present simplified description and is only amenable to numerical solutions. In the following, we will therefore continue with the qualitative, but analytical, solution of the elementary model for gobbling.

3.4. *From gobbling to jetting*

The simple dynamic model describes successfully a single gobbling cycle. However, in order to obtain a periodic behaviour, the integral over the period $\int_0^T U_d(t)\,dt$ should be equal to δL, the difference between the detachment length and the jet length at the start of the next cycle. The analysis of the video images shows that this difference is on the order of the diameter of the terminal drop before its detachment, which is relatively small compared to the large breakup length L_{max} observed for fully developed gobbling. If we neglect this variation, then the periodicity condition becomes

$$\int_0^T U_d(t)\,dt \cong 0. \tag{3.17}$$

Notice that this condition implies $U_d(t) < 0$ in the initial part of the period, which, according to (3.13), leads to $U_0 < U^*$, i.e. $We < 1$. This inequality is in apparent contradiction with the requirement of a positive downstream momentum flux in the jet. However, the small, but non-negligible, contribution of gravity solves this apparent paradox and allows a polymeric jet to exist down to flow rates Q_{cr} and below the critical flow rate Q_{cr0} as described in § 3.2.

The periodicity condition (3.17) in combination with (3.13) leads to the following expression for the gobbling period:

$$T = \frac{6(U^* - U_0)}{g}. \tag{3.18}$$

The amplitude of the oscillation ΔL can be evaluated from the minimum jet length L_{min} which occurs at $t = T/2$:

$$\Delta L = L_{max} - L_{min} = \frac{3(U^* - U_0)^2}{2g}. \tag{3.19}$$

This oscillation amplitude determines the range and the different stages of the gobbling regime. Indeed, *incipient*, *moderate* and *critical* gobbling states, as already introduced from observation in figure 3, correspond to $\Delta L = 0$, $L_{max}/2$ and L_{max}, respectively. The condition for *incipient* gobbling is straightforward: this stage appears as $U_0 = U^*$, i.e. $Q = Q_{cr0}$ or $We = 1$. This condition is in agreement with the experiment displayed in figure 3 where incipient gobbling indeed corresponds to $We \simeq 1$.

Determining the lower bound of flow rates for which periodic gobbling persists (corresponding to *critical* gobbling) requires knowledge of the maximum length L_{max}. We therefore assume in the following that L_{max} is defined by the breakup time t_{br} of the elastic filament connecting the drop to the jet, such as

$$L_{max} = t_{br} U_0. \tag{3.20}$$

The lower limit U_{crit} in the range of possible jet velocities for gobbling, $U_{crit} < U_0 < U^*$, is then determined by the requirement $\Delta L = L_{max}$, which, according to (3.19), leads to:

$$U_{crit} = U^* \left(1 + \tfrac{1}{3}\epsilon - \sqrt{\tfrac{2}{3}\epsilon + \tfrac{1}{9}\epsilon^2} \right); \quad \epsilon = \frac{g t_{br}}{U^*}. \tag{3.21}$$

The gobbling regime occurs over a narrow range of flow rates just below U^*, which vanishes if the breakup time decreases down to the value characteristic of a Newtonian liquid or if the nozzle radius becomes very small.

The narrow range of flow rates for gobbling can be demonstrated by plotting the volume $\mathscr{V}_{max}$ of the terminal drop when detaching from the jet as a function of the jet velocity as displayed in figure 10. Following our simplified model, the combination of (3.16) with (3.18) leads to

$$\mathscr{V}_{max} = 6\pi R_0^2 U_0 \left(\frac{U^* - U_0}{g} \right). \tag{3.22}$$

In spite of the experimental scatter of the data in figure 10 (which we believe to be due to the high sensitivity to the rheological properties of the liquid) this relation is in reasonably good agreement with the experiments, conducted here with a particular nozzle radius $R_i = 0.075$ mm. Equation (3.22) contains no adjustable parameters. Over the narrow range of experimentally observed velocities of $\Delta U_0 = U^* - U_{crit} = (0.84 - 0.62)\,\mathrm{m\,s^{-1}}$, all stages of gobbling that are depicted in figure 3, from incipient to critical gobbling, can be observed. Finally, an estimation of the breakup time t_{br} can be
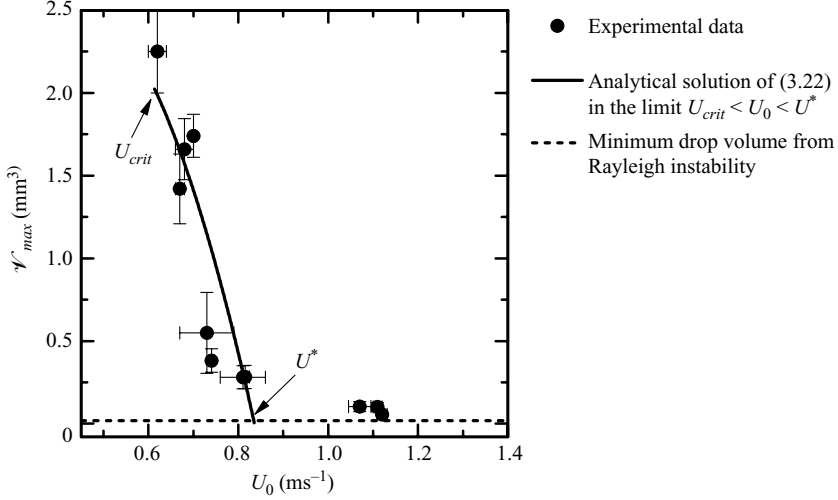
FIGURE 10. Gobbling range: terminal drop volume at detachment $\mathcal{V}_{max}$ versus jet velocity U_0. Points: experimental data for $R_i = 0.075$ mm; solid line: theory according to (3.22).

determined from this velocity range by measuring the lower bound U_{crit} and rewriting (3.21), which reduces for small radii and smaller values of ϵ to $U_{crit} = U^*(1 - \sqrt{2/3\epsilon})$ and we obtain

$$t_{br} \cong \frac{3(U^* - U_{crit})^2}{2gU_{crit}}. \qquad (3.23)$$

We experimentally measured $U_{crit} \simeq 0.62$ m s^{-1}, which would correspond to $t_{br} \simeq 11$ ms for the nozzle radius used in these experiments. In the following section, we describe the variation of this breakup time with the nozzle radius and show the consistency of a calculation of t_{br} from L_{max}/U_0 with the above estimation from U_{crit}.

3.5. *The breakup time*

In the previous sections we have shown the relevance of the simplified dynamical model to describe the gobbling phenomenon. However, we had to introduce a breakup time t_{br} as an adjustable parameter. Determining the dependence of t_{br} on the experimental parameters is still required to close this dynamical model. We first note that t_{br} is in fact an apparent breakup time defined as L_{max}/U_0 in (3.20). In reality, the fluid also accelerates under gravity and the actual time of flight of a Lagrangian fluid particle $t_{of} = \int_0^{L_{max}} \mathrm{d}z/U(z)$ is smaller than t_{br}. This time of flight can be evaluated using the numerical velocity profiles obtained from integrating equation (B 3) of the dynamic theory in Appendix B.

Both the apparent breakup time and the time of flight were estimated from the maximum jet length L_{max} extracted from processing the XLt diagrams. The variation of these breakup times as a function of the nozzle radius is displayed in figure 11. Both measures of the breakup time are found to increase with the radius of the nozzle. The results for t_{br} are fairly well described by a linear correlation (solid line in figure 11) that has the following form for the present polymer solution and test geometry:

$$t_{br} \text{ (s)} = 0.14R_i \text{ (mm).} \qquad (3.24)$$

The breakup time corresponding to the nozzle radius presented in the previous section ($R_i = 0.075$ mm) is 10.5 ms, which is in relatively good agreement with the value estimated from the experimental measurement of U_{crit} ($t_{br} \simeq 11$ ms). The linear
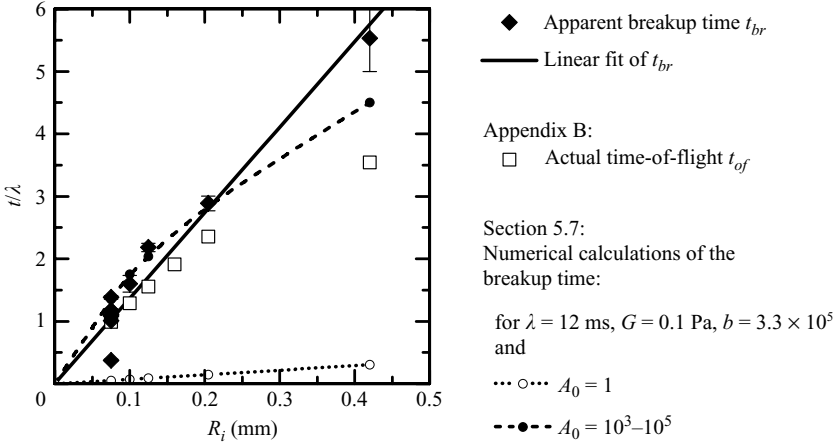
FIGURE 11. Apparent breakup time $t_{br} = L_{max}/U_0$ (◆) fitted by (3.24) (solid line); actual time-of-flight t_{of} (□) for an accelerating jet (Appendix B); and theoretically predicted breakup times from §4.7 (dashed and dotted line).

correlation is surprising since it suggests that the breakup dynamics are limited by viscosity $t_{br} \sim \eta R_0/\gamma$ (this scaling arises from a simplified balance between the destabilizing Laplace pressure ($\sim \gamma/R_0$) with viscous stresses resisting breakup ($\sim \eta/t_{br}$) (Eggers 1997). However, the equivalent viscosity would need to be of the order of 2 Pa.s to match our empirical correlation, which is 3 orders of magnitude higher than the actual shear viscosity of the dilute polymeric solutions. Such high values are the signature of strong elastic stresses generated in the fluid while the filament thins. Indeed, the extensional viscosity of polymeric solutions commonly increases over several orders of magnitude during strong elongational flows (McKinley & Sridhar 2002; Amarouchene *et al.* 2001; Sattler *et al.* 2008).

3.6. *Predicting critical gobbling parameters*

Substituting the empirical correlation (3.24) for the breakup time obtained with the present polymer solution in the relation (3.21) closes the description of the gobbling dynamics. The lower critical velocity U_{crit} that relates to critical gobbling (as shown in figure 3) and the corresponding flow rate,

$$Q_{crit} = \pi R_0^2 U_{crit}, \tag{3.25}$$

can then be evaluated. In figure 12 we compare the critical flow rates of the theoretical predictions of incipient and critical gobbling, calculated without any fitting parameter (besides the linear correlation between t_{br} and the nozzle radius R_i), with experimental data close to critical gobbling conditions. The experimental data are indeed close to the theoretical predictions of critical gobbling (solid line). The deviation is due to the fact that experimental data are still obtained at flow rates slightly higher than critical gobbling conditions (this can also be seen in figure 3 where, for the indicated case of critical gobbling, the terminal drop is actually not travelling completely back to the nozzle). Flow rates right at critical gobbling present a rather unstable state that favours a reconnection of the terminal drop to the nozzle even with very small flow rate variations. Figure 12 also shows the results of the numerical calculations of the dynamic theory of Appendix B for the range of incipient to critical gobbling.

The lower critical velocity U_{crit} of (3.21) can also be used to calculate the volume of the detaching terminal drop $\mathcal{V}_{max}$. By inserting U_{crit} into (3.22) we obtain the volume
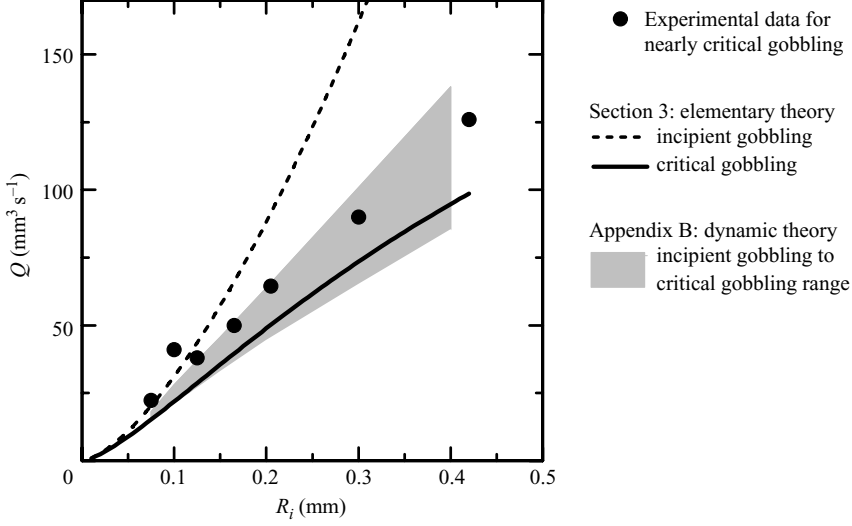
FIGURE 12. Critical flow rates as a function of the inner radius of the nozzle: (●) experimental data for PAA solutions close to critical gobbling conditions; dashed line: elementary theory of §3.3 for incipient gobbling (Q_{cr0}) from (3.9); solid line: elementary theory of §3.3 for critical gobbling Q_{crit} from (3.25); shaded area: range of critical flow rates based on the dynamic theory of Appendix B for incipient to critical gobbling.

of the detaching terminal drop at critical gobbling conditions:

$$\mathscr{V}_{crit} = 6\pi R_0^2 U_{crit} \left(\frac{U^* - U_{crit}}{g} \right). \tag{3.26}$$

This theoretical prediction for the critical volume of the terminal drop is plotted in figure 13 as the solid line and shows very good agreement with the experimentally obtained values. This drop volume $\mathscr{V}_{crit}$ can also be compared to the volume of a quasi-static dripping drop detaching from a syringe tip. The latter situation has been comprehensively studied by Harkins and Brown (Harkins & Brown 1919) and constitutes a common method to estimate interfacial tensions (Adamson & Gast 1997). Harkins and Brown have shown that the volume of the detaching drop is given by

$$\mathscr{V}_{drip} = f_{HB} \frac{2\pi \gamma R_e}{\rho g}, \tag{3.27}$$

where R_e is the external radius of the tip and f_{HB} is a function of the ratio $X = R_e / \sqrt{\gamma / \rho g}$ ranging from $0.5 \leqslant f_{HB} \leqslant 1$. The coefficient f_{HB} accounts for the non-sphericity of a terminal drop due to gravity. The 'smoothed values recommended for corrections' by Harkins and Brown are well approximated by a polynomial fit:

$$f_{HB} \simeq 0.928 - 0.7847X + 0.7025X^2 - 0.2233X^3; \quad X = \frac{R_e}{\sqrt{\gamma / \rho g}}, \tag{3.28}$$

in the range $0 < X < 1.4$. As illustrated in figure 13 the volume $\mathscr{V}_{crit}$ of the terminal gobbling drops at critical conditions are significantly below the volume $\mathscr{V}_{drip}$ of the Harkins–Brown relation for dripping, but also much larger than the volume of detaching drops for the jetting case $\mathscr{V}_\mu$ (obtained from (3.31) as we describe below). This difference in volume between dripping and gobbling explains also why the critical gobbling conditions are so sensitive to slightest variations in the flow rate: a slight
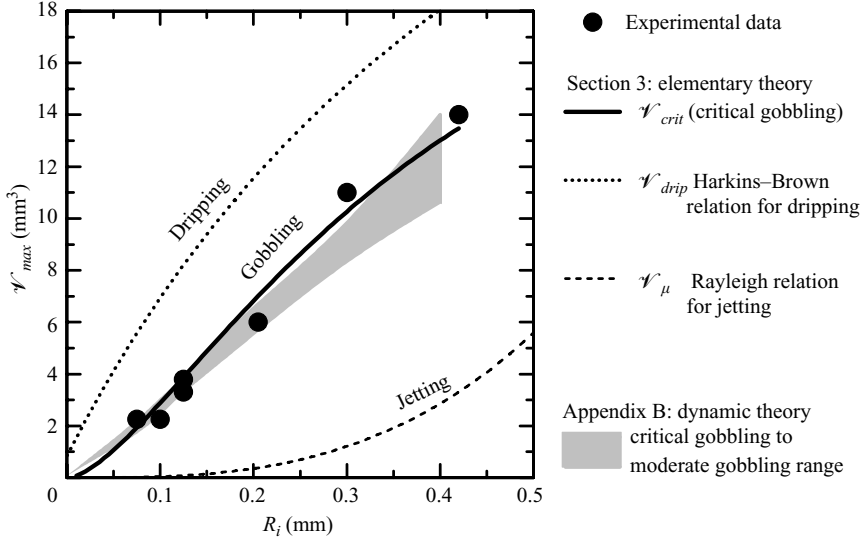
FIGURE 13. Variation in maximum drop volume versus nozzle radius. Here, (●) represents experimental data close to critical gobbling conditions; solid curve: prediction for critical gobbling based on (3.26) of the elementary theory of §3.3; dotted line: drop volume for dripping predicted using the Harkins–Brown relation (3.27); dashed line: drop volume predicted for jetting using the Rayleigh relation (3.31); shaded area: predictions of the dynamic theory of Appendix B for critical to moderate gobbling.

decrease in flow rate will lead to reattachment of the terminal drop to the nozzle (shown in figure 3 as 'intermittent gobbling'). This then prohibits the continuation of the gobbling cycle since $\mathscr{V}_{crit}$ is not large enough for pinch off due to dripping. The terminal drop attached to the nozzle first has to grow (by inflow of fluid) to reach the Harkins–Brown volume condition $\mathscr{V}_{drip}$ in order to detach again.

The dependence of $\mathscr{V}_{crit}$ on R_i for the experimental data shown in figure 13 is found to be almost linear over this range of nozzle diameters and can be approximated by

$$\mathscr{V}_{crit} \simeq 0.8 \frac{2\pi\gamma R_i}{\rho g} \simeq 0.7 \frac{2\pi\gamma R_0}{\rho g}, \tag{3.29}$$

where the latter equality is obtained by using (2.2). This simple relation will be used in the following section to determine an upper bound on the range of syringe nozzles for which the development of the gobbling regime can be observed.

3.7. *Limits of gobbling*

As observed in figures 1 and 3, the jet exiting the nozzle first undergoes a classical Rayleigh–Plateau instability controlled by the interplay of inertia and capillarity, leading to the beads that are eventually consumed by the terminal drop. A linear perturbation calculation gives the wavelength of the fastest growing mode (Rayleigh 1879, 1892; Weber 1931):

$$L_R = 2\sqrt{2}\pi R_0 \simeq 9.0 R_0, \tag{3.30}$$

the volume:

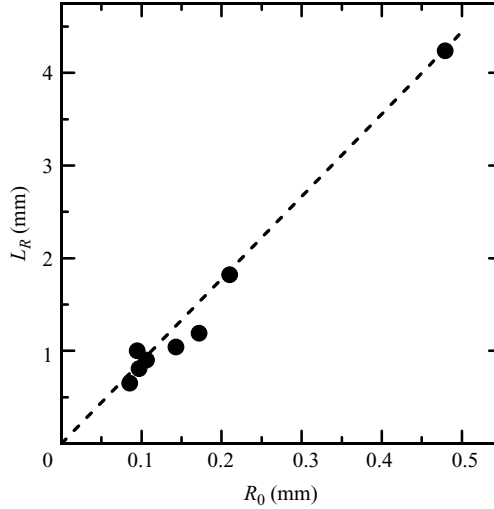$$\mathscr{V}_\mu = \pi L_R R_0^2 = 2\sqrt{2}\pi^2 R_0^3, \tag{3.31}$$

FIGURE 14. Wavelength of the beads observed on the jets in figure 1 as function of the jet radius. Dashed line: comparison with Rayleigh theory (3.30).

and the corresponding time scale:

$$\tau_R \simeq 2.9 \sqrt{\frac{\rho R_0^3}{\gamma}}. \qquad (3.32)$$

The wavelength L_R determined from the video images was measured for different column radii and is compared with the Rayleigh prediction in figure 14. The agreement between the experimental data and the classical prediction is very good, which indicates that the presence of minute quantities of polymer molecules does not modify the initial inertiocapillary dynamics controlling the formation of the beads. Indeed typical values for the inertial time characterizing the growth rate of the inertiocapillary perturbation ($\tau_R \sim 1\,\mathrm{ms}$) are shorter than the fluid relaxation time ($\lambda \sim 10\,\mathrm{ms}$) which characterizes the time scale for growth of viscoelastic stresses. In the linear regime (at short times) polymer effects are negligible. Of course, this situation changes dramatically in the nonlinear regime (Amarouchene *et al.* 2001; Wagner *et al.* 2005). The volume V_μ of a single bead represents the lower limit for the terminal gobbling drop when reaching the transition to pure jetting and is also compared in figure 13 to the critical gobbling conditions.

The number of beads consumed by the terminal drop per gobbling period is given by the ratio of the maximum volume of the terminal drop to that of a single bead. From (3.29) and (3.31) we obtain for the 'gobbling ratio':

$$\frac{\mathscr{V}_{crit}}{\mathscr{V}_\mu} \approx 0.16 \left(\frac{\gamma}{\rho g R_0^2} \right) \approx 0.11 \left(\frac{\gamma}{\rho g R_i^2} \right). \qquad (3.33)$$

The 'gobbling ratio' scales inversely with the Bond number, which explains why it increases dramatically for thin jets as the velocity approaches the critical value (e.g. for $R_i = 0.1\,\mathrm{mm}$ we obtain $\mathscr{V}_{crit}/\mathscr{V}_\mu \sim 50$). In the opposite limit, the 'gobbling ratio' approaches unity for $R_{cr} \approx \sqrt{0.11\gamma/\rho g} = 0.8\,\mathrm{mm}$: above this critical radius the gobbling phenomenon should not be observable because formation of a single bead on the jet is sufficient to overwhelm the volume of the terminal drop.
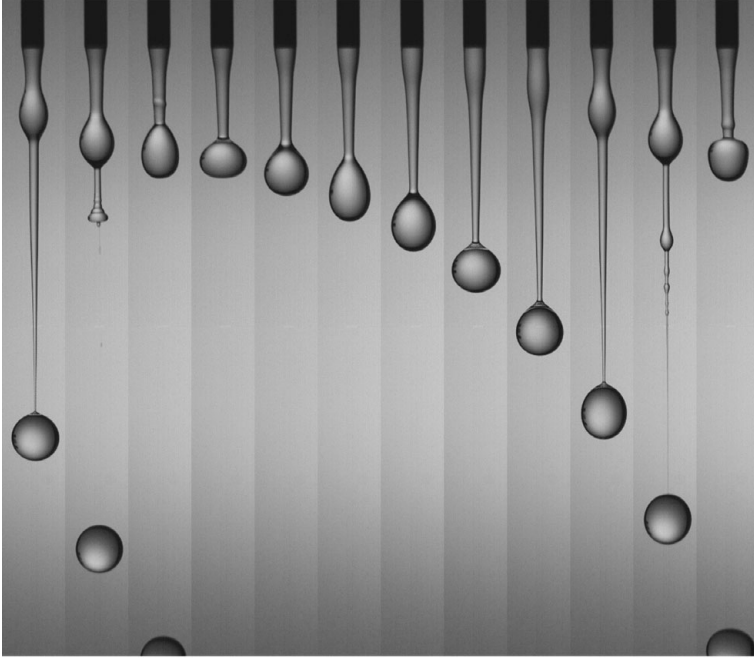
FIGURE 15. False gobbling: periodic dripping with consecutive drops connected by an 'umbilical cord', $R_i = 0.685$ mm; $Q = 160$ mm^3 s^{-1}.

Although preliminary investigations suggest that the gobbling phenomenon also seems to occur for jets of larger diameter, closer observation reveals that these jetting flows differ from 'true gobbling'. For larger nozzle radii, the transition from dripping to jetting for a polymer solution proceeds through a stage of interacting drops or beads-on-a-string: as a result of the enhanced stability of the necks between the drops that form at large radii (see figure 15), the next drop begins to mature before the leading drop has detached. A detailed analysis of video images shows that, in this case, the motion of the 'leading drop' affects the dynamic behaviour of the rest of the jet through the tension transmitted along the thin umbilical cord of highly stretched fluid that can be observed in figure 15.

The four XLt diagrams of figure 16 illustrate this issue; they represent the near-critical gobbling regimes for thin ($R_i = 0.125$ mm) to wide ($R_i = 0.685$ mm) nozzles. Figure 16(a) shows true gobbling with multiple beads (gobbling ratio $\mathcal{V}_{crit}/\mathcal{V}_{\mu} \sim 38$) merging into a single terminal drop which follows the expected parabolic trajectory. Figures 16(b) and 16(c) still correspond to gobbling, but lower gobbling ratios of $\mathcal{V}_{crit}/\mathcal{V}_{\mu} \sim 9$ and ~ 3, respectively, as the nozzle radius increases. In figure 16(d) necklaces of drops connected by thin fluid filaments are observed: the next drop emerges and starts to grow before the connecting ligament has broken up and the first terminal drop has detached. We refer to this as 'false gobbling'. Essentially, it represents periodic dripping with consecutive drops connected by an 'umbilical cord' as can be seen in figure 15. The most important dynamic difference is that in this case gravity is essential; the tensile force in the jet (arising now principally from elasticity) is transmitted upstream up to the nozzle; whereas for true gobbling, the force originates solely from capillarity at the nozzle. True gobbling dynamics for such large nozzle radii could only occur in reduced or microgravity conditions.
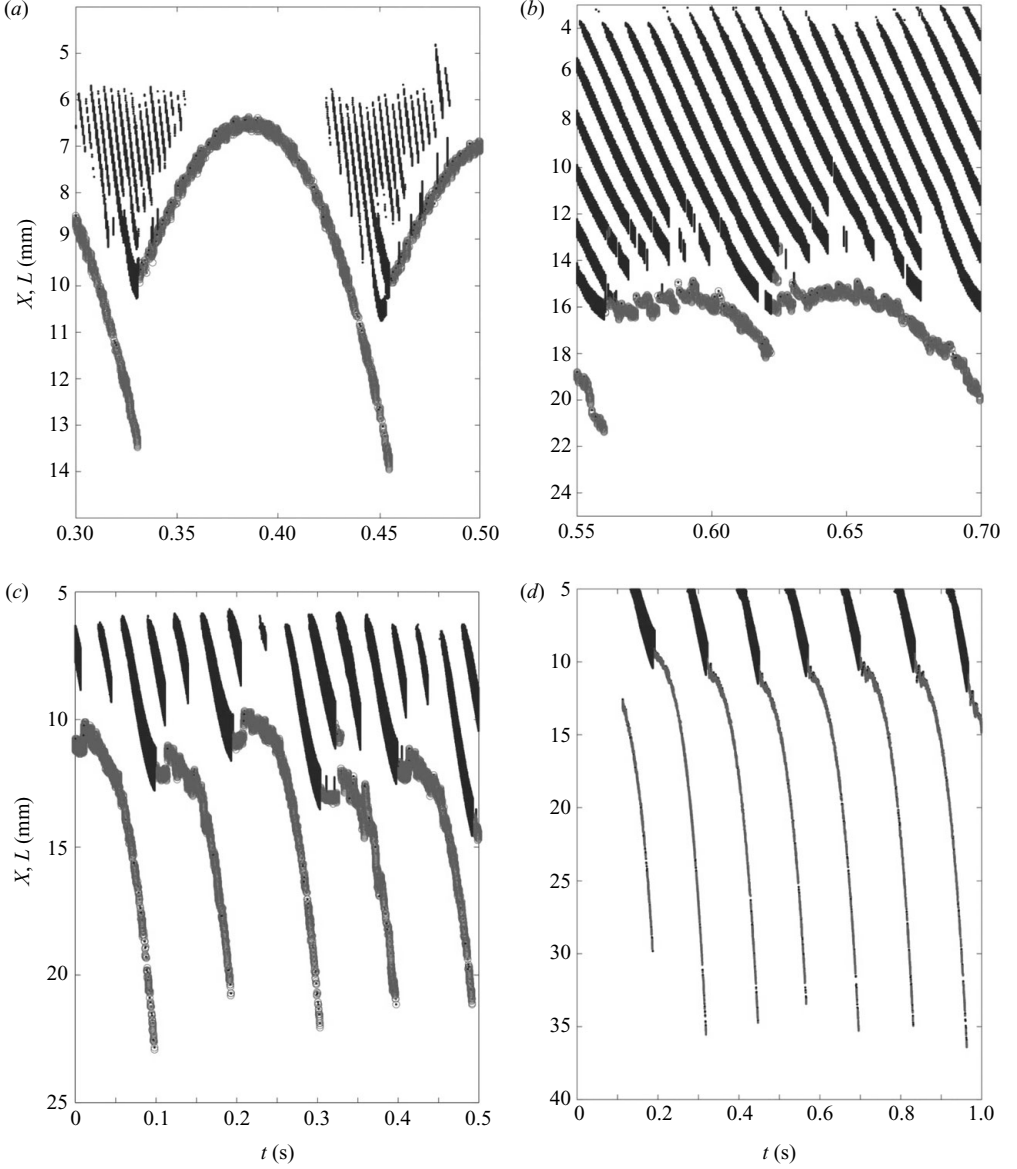
FIGURE 16. XLt diagrams showing transition from gobbling to dripping: (a): $R_i = 0.125$ mm, $Q = 39.7$ mm^3 s^{-1}, gobbling ratio ~ 38; (b): $R_i = 0.205$ mm, $Q = 64.5$ mm^3 s^{-1}, gobbling ration ~ 9; (c): $R_i = 0.42$ mm, $Q = 140$ mm^3 s^{-1}, gobbling ratio ~ 3; (d): $R_i = 0.685$ mm; $Q = 160$ mm^3 s^{-1}, periodic dripping: necklace of drops.

4. Ligament thinning and breakup time

Good agreement is obtained between the predictions of the simple elementary and dynamic theories and the experimental results for Q_{crit} and $\mathcal{V}_{crit}$ shown in figure 12 and 13. This suggests that the main features of the gobbling phenomenon are governed by fundamental mass and momentum balances, while the polymer additive controls only the terminal drop detachment event, which is encoded implicitly in the breakup time given by (3.24). However, delayed breakup times are essential for the
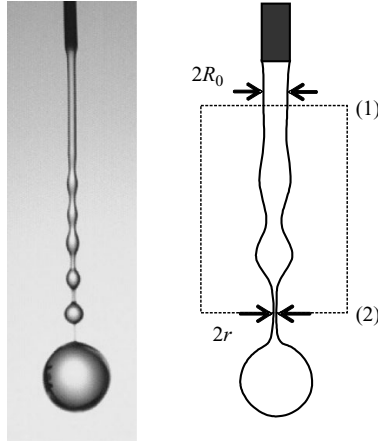
FIGURE 17. Control volume for a viscoelastic steady jet issuing from a nozzle.

occurrence of the gobbling phenomenon (in Clanet & Lasheras 1999 the breakup time of pure water is simply too short to observe gobbling). We discuss in this section the dependence of the breakup time on the nozzle radius and the viscoelastic characteristics of the polymer additive.

The elementary dynamical model presented in the previous sections used an apparent breakup time t_{br}, or equivalently a maximum jet length L_{max}, measured experimentally to incorporate the effects of the dissolved polymer. For a quantitative description of the influence of the polymeric additive, we analyse now the thinning and breakup of the thin ligaments that interconnect the beads-on-string structure and which develop due to capillary instability of the primary jet. This simple zero-dimensional theory follows a similar form to the theory developed for capillary thinning of filaments of polymeric fluids in the Capillary Breakup Extensional Rheometer (see Bazilevskii *et al.* 1990*a*; Entov & Hinch 1997; Anna & McKinley 2001; Rozhkov 1983). However, the present description involves one major new element: the ligament is submitted to a constant axial force.

We first note that the ligaments start as necks between adjacent beads on the jet which grow and become visible at some distance from the nozzle. Because the beads and ligaments are convected along the jet, each ligament is a Lagrangian object consisting of the same fluid particles. As each ligament is convected downstream, it progressively thins and has two possible fates: (i) it can reach the terminal drop and be consumed by it, or (ii) it can break and the terminal drop thus detaches. The video images of the ligaments show that they are elongated and uniform cylindrical threads. It is therefore reasonable to consider the thinning ligament as a uniformly stretching liquid column aligned along the jet axis.

4.1. *Force in the ligament and equation for elastocapillary thinning*

Following our previous elementary discussion, we first neglect the effect of gravity and consider a short fast jet, with a uniform velocity U_0. We choose two cross-sectional profiles of the jet as shown in figure 17, the first (1) being located at a stationary location just downstream of the nozzle exit within the fully developed uniform jet region, and the second (2) moving at the velocity of the central Lagrangian element of a thinning ligament. Within these boundaries, the time-averaged value of the linear momentum within any control volume between two jet cross-sections remains

constant. Therefore, the time-averaged momentum flux $-F + \rho Q U_0$ as defined in the first two terms of the momentum balance (3.3) is also constant along the jet. The time-averaging implicit in this expression relates to averaging over a time interval large when compared with the characteristic time scale of capillary breakup (the Rayleigh time), and with the time interval between two beads passing across any given cross-section. In the fully developed gobbling regime such an interval is small with respect to the overall gobbling period.

As the product $\rho Q U_0$ is constant, the net tensile force F acting on any cross-section is also uniform along the jet. This *constant force* throughout the jet is readily evaluated from (3.6) if we replace the upstream radius R_0 with the radius $r(z)$:

$$F = \pi r \gamma + \pi r^2 \sigma_{rheol} = constant. \tag{4.1}$$

This force is the sum of a capillary surface force and a bulk viscoelastic force arising from the stretching of the dilute polymeric solute. The value of this constant force can be evaluated from the upstream cross-section (1) where the rheological stress is negligible:

$$F = \pi R_0 \gamma. \tag{4.2}$$

We equate these two expressions to obtain the following expression for the tensile rheological stress difference that develops in the thinning filament:

$$\sigma_{rheol} = \frac{\gamma}{r} \left(\frac{R_0}{r} - 1 \right). \tag{4.3}$$

The rheological stress σ_{rheol} developed in polymer solutions consists of two principal contributions, namely a viscous stress proportional to the instantaneous strain rate, and an elastic stress depending on the accumulated elastic (reversible) strain of the polymer. We will confine our present analysis to dilute polymer solutions for which the additional contribution to the total viscous stress is small, while the elastic stress becomes significant when large elastic strains are reached.

4.2. FENE model for dilute polymer solutions

In order to analyse the ligament thinning we use the same constitutive model as Entov & Hinch (1997), corresponding to a dilute suspension of dumbbells with a finite polymer extensibility (the FENE dumbbell model (Bird, Armstrong & Hassager 1987)). The elastic deformation in the jet, described by the average second moment configuration tensor $\boldsymbol{A}$ of the polymer, is characterized by its axial (A_{zz}) and radial (A_{rr}) components which are governed by the microstructural evolution equations:

$$\dot{A}_{zz} = 2e_{zz} A_{zz} - \frac{f}{\lambda}(A_{zz} - 1); \quad \dot{A}_{rr} = 2e_{rr} A_{rr} - \frac{f}{\lambda}(A_{rr} - 1). \tag{4.4}$$

Here, e_{zz} and e_{rr} are the axial and radial components of the strain rate tensor, λ is the fluid relaxation time and f is the FENE correction term accounting for finite extensibility of the polymeric molecules:

$$f = \frac{1}{(1 + 3/b) - (A_{zz} + 2A_{rr})/b}. \tag{4.5}$$

A_{zz} is essentially the square of the ratio of the current length of the extended polymer molecule to its initial length in the coiled state, the finite extensibility parameter b corresponds to the limit of A_{zz} at the maximum extension of the polymer chain. The resulting viscoelastic stress contributions for this FENE dumbbell model are

$$\sigma_{zz} = 2\eta e_{zz} + Gf(A_{zz} - 1); \quad \sigma_{rr} = 2\eta e_{rr} + Gf(A_{rr} - 1), \tag{4.6}$$

where G is the elastic modulus of the fluid. The components of the strain rate tensor for thinning of the filament are expressed in terms of the rate of evolution in the filament radius:

$$e_{zz} = -\frac{2\dot{r}}{r}; \quad e_{rr} = \frac{\dot{r}}{r}. \tag{4.7}$$

In contrast to the derivation of Entov & Hinch (1997) for a stationary filament under zero tensile force, for the case of a jet we are now taking the constant force into account. Therefore we are substituting in (4.3) the rheological stresses $\sigma_{rheol} = (\sigma_{zz} - \sigma_{rr})$ with (4.6) and (4.7). Introducing then (4.7) also into (4.4) we get the following set of ordinary differential equations:

$$6\eta \left(\frac{\dot{r}}{r}\right) = -\frac{\gamma R_0}{r^2} + \frac{\gamma}{r} + f G (A_{zz} - A_{rr}); \tag{4.8a}$$

$$\dot{A}_{zz} + 4\left(\frac{\dot{r}}{r}\right) A_{zz} = -\frac{f}{\lambda}(A_{zz} - 1); \tag{4.8b}$$

$$\dot{A}_{rr} - 2\left(\frac{\dot{r}}{r}\right) A_{rr} = -\frac{f}{\lambda}(A_{rr} - 1). \tag{4.8c}$$

It should be noted that in (4.8a), by contrast to the capillary breakup described by Entov & Hinch (1997), the constant force acting along the jet enters as the additional term $\gamma R_0 / r^2$ in the force balance on the thinning ligament. This set of equations can be solved numerically with the appropriate initial conditions, $r = R_0$; $A_{zz} = A_{rr} = 1$ at $t = 0$, to predict the evolution of the ligament radius in a jet with a persistent constant axial force as material elements are convected along the jet. However, before presenting numerical results, it is worth discussing the general features of the solutions.

4.3. *First stage of thinning: inertiocapillary equilibrium*

As described in §3.7, the jet first undergoes a Rayleigh–Plateau instability with a characteristic time scale $\tau_R \simeq 2.9\sqrt{\rho R_0^3 / \gamma}$. During this first stage, the necking dynamics from an arbitrary small perturbation α follow an exponential growth $r = R_0(1 - \alpha e^{t/\tau_R})$, which induces a local strain rate near the neck of the form

$$e_{zz} = \frac{2}{\tau_R} \frac{\alpha e^{t/\tau_R}}{1 - \alpha e^{t/\tau_R}}. \tag{4.9}$$

The axial extension rate thus increases rapidly, which induces stretching of the polymer molecules and leads to a elastocapillary regime in which the elastic response of the fluid dominates its inertia.

4.4. *Second stage of thinning: elastocapillary equilibrium. Infinite extensibility*

In the elastocapillary regime we assume that the axial elastic strain of the polymer is large, $A_{zz} \gg 1$; $A_{zz} \gg A_{rr}$. We also assume that the molecules are very extensible so that $A_{zz} \ll b$ and $f \approx 1$. Equation (4.8) reduces then to

$$6\eta \left(\frac{\dot{r}}{r}\right) = -\frac{\gamma R_0}{r^2} + \frac{\gamma}{r} + G A_{zz}; \tag{4.10a}$$

$$\dot{A}_{zz} + 4\left(\frac{\dot{r}}{r}\right) A_{zz} = -\frac{1}{\lambda} A_{zz}. \tag{4.10b}$$

Equation (4.10b) is readily integrated, assuming that the filament radius and the axial component of the elastic strain satisfy the relation $A_{zz} r^4 = A_{zz}^0 R_0^4$, since the Rayleigh time scale $\sqrt{\rho R_0^3 / \gamma}$ is much smaller then polymer relaxation time λ, and therefore

no relaxation of the polymer occurred during the previous inertiocapillary thinning stage. Taking the initial value of the axial stretch of the polymer (A_{zz}^0) equal to unity, integration of (4.10b) gives

$$A_{zz}r^4 = R_0^4 \exp(-t/\lambda). \qquad (4.11)$$

Introducing this expression into (4.10a) we find

$$6\eta \left(\frac{\dot{r}}{r}\right) = -\frac{\gamma R_0}{r^2} + \frac{\gamma}{r} + \frac{GR_0^4}{r^4} \exp\left(-\frac{t}{\lambda}\right). \qquad (4.12)$$

As the radius $r(t) \to 0$, a dominant balance is established between the first and third term on the right-hand side of (4.12). At long times the solutions thus approach exponential asymptotes:

$$\frac{r}{R_0} \sim \sqrt{\frac{GR_0}{\gamma}} \exp\left(-\frac{t}{2\lambda}\right); \quad A_{zz} = \left(\frac{\gamma}{GR_0}\right)^2 \exp\left(\frac{2t}{\lambda}\right). \qquad (4.13)$$

These expressions in (4.13) correspond to an intermediate asymptotic regime of quasi-equilibrium elastocapillary thinning of a filament of viscoelastic fluid in a jet under a constant axial force $\pi\gamma R_0$. The filament radius exponentially tends to zero while the elastic stretch in the polymer molecules increases exponentially with time; however, the scaling is different in comparison to elastocapillary thinning in the absence of a constant force for which $r(t) \sim \exp(-\frac{t}{3\lambda})$ (Entov & Hinch 1997).

This solution also implies that the ligament will not breakup in a finite time and the elastic stress grows without bound. However, as the polymeric stretch increases, finite extensibility effects eventually become important and need to be taken into account. The intermediate elastocapillary solution (4.13) can only be used until the ratio A_{zz}/b becomes significant, typically $A_{zz}/b \approx 0.1$. After that, the thinning dynamics and the final breakup are determined by the finite extensibility of the polymer.

4.5. *Third stage of thinning: finite extensibility and breakup*

In the very final stage of ligament thinning under a constant axial force, the elastic strain is very large, the radius is very small and (4.8) simplifies to:

$$6\eta \left(\frac{\dot{r}}{r}\right) = -\frac{\gamma R_0}{r^2} + fGA_{zz}; \qquad (4.14a)$$

$$\dot{A}_{zz} + 4\left(\frac{\dot{r}}{r}\right)A_{zz} = -\frac{f}{\lambda}A_{zz}; \quad f = \frac{b}{b - A_{zz}}. \qquad (4.14b)$$

We neglect the term $6\eta\dot{r}/r$, assuming viscosity to be small. Then we get from (4.14a):

$$\frac{r}{R_0} = \sqrt{\frac{\gamma}{GR_0}}\sqrt{\frac{1}{A_{zz}} - \frac{1}{b}}; \quad \frac{\dot{r}}{r} = -\frac{1}{2}\frac{\dot{A}_{zz}}{A_{zz}}\left(\frac{1}{1 - \frac{A_{zz}}{b}}\right). \qquad (4.15)$$

Introducing these expressions into (4.14b) and integrating we find an implicit expression which describes the universal thinning behaviour close to breakup:

$$\frac{t}{\lambda} = \frac{A_{zz}}{b} + \ln\frac{A_{zz}}{b}. \qquad (4.16)$$

The evolution in radius with time can be found by substituting the implicit expression (4.16) in (4.15). The above estimates demonstrate that in the case of very thin jets, or very dilute polymer solutions with molecules only having moderate extensibility the intermediate exponential thinning stage may be absent, so that the third stage of

dominating finite extensibility effects may become important immediately after the initial thinning stage (see, for example, Clasen *et al.* 2006*b*).

It should be noted that the expressions derived above can be generalized to describe the thinning of a liquid filament extended by any constant force F. The first term of the right-hand side of (4.8*a*) reads then $-F/\pi r^2$ and we obtain a solution for the radius evolution during the second stage of elastocapillary thinning from (4.13):

$$\frac{r}{R_0} = \sqrt{\frac{G\pi R_0^2}{F}} \exp\left(-\frac{t}{2\lambda}\right) \tag{4.17}$$

and for the third stage from (4.15):

$$\frac{r}{R_0} = \sqrt{\frac{F}{G\pi R_0^2}} \sqrt{\frac{1}{A_{zz}} - \frac{1}{b}}. \tag{4.18}$$

4.6. *Calculating the evolution in ligament radius*

The results presented above allow us to predict the evolution in the ligament radius and thus the critical time to breakup t_{br} as a function of the initial jet radius R_0 and measurable fluid properties. If the duration of the short initial stage is neglected, the thinning kinetics are completely determined by the fluid relaxation time λ, the surface tension γ, the elastic modulus G of the fluid, the finite extensibility parameter b of the polymer and the jet radius R_0. The elastic modulus G of dilute polymer solutions is small and cannot readily be measured directly, but can be estimated using the well-known expression from kinetic theory (Bird *et al.* 1987) $G = 3nk_BT$. Here, $n = cN_A/M_w$ is the number density of polymer molecules of the solution, k_B is the Boltzmann constant and T is the absolute temperature. In our case, with $c = 100$ ppm and $M_w \sim 7.5 \times 10^6$ g mol^{-1} we obtain $n \sim 8 \times 10^{12}$ cm^{-3} and $G \sim 0.1$ Pa. This value should be regarded as an order-of-magnitude estimate. The finite extensibility parameter b can be estimated from the number of Kuhn-steps in a polymer chain, $b = 3N_K$. For polyacrylamide we obtain $b \approx 3.3 \times 10^5$.

Predictions for the kinetics of ligament thinning and breakup in the jet are then obtained by integrating (4.8) using these fluid properties. Results for the evolution in ligament radius for the range of nozzle radii R_0 used in experiments are shown in figure 18(*a*). The broken line shows predictions of the asymptotic theory for the intermediate quasi-equilibrium elastocapillary regime from (4.13). However, for the molecular parameters relevant to our polyacrylamide chains, finite extensibility affects the kinetics of constant-force thinning almost from the beginning, leading to faster thinning than the exponential equilibrium as can be seen in figure 18(*a*).

Some general conclusions follow from these results. For a fixed relaxation time, the breakup time depends on the initial radius of the ligament and on the macromolecular extensibility. The dependence on the initial radius can be traced back to the equality $A_{zz}r^4 = A_{zz}^0 R_0^4$ which gives the value of elastic strain at the end of the initial fast necking phase when we cross over from the inertiocapillary to the elastocapillary regime. From (4.13), this strain scales as R_0^{-2}, which leads to a prolonged stage of elastocapillary thinning in the ligament for larger R_0. This provides a preliminary explanation of the increasing longevity of the ligaments in the gobbling regime for larger nozzle sizes.

4.7. *Breakup time: theory versus experiment*

We are finally in a position to evaluate the jet breakup time t_{br} as a function of the initial jet radius by calculating the evolution of the ligament radius from R_0 to breakup
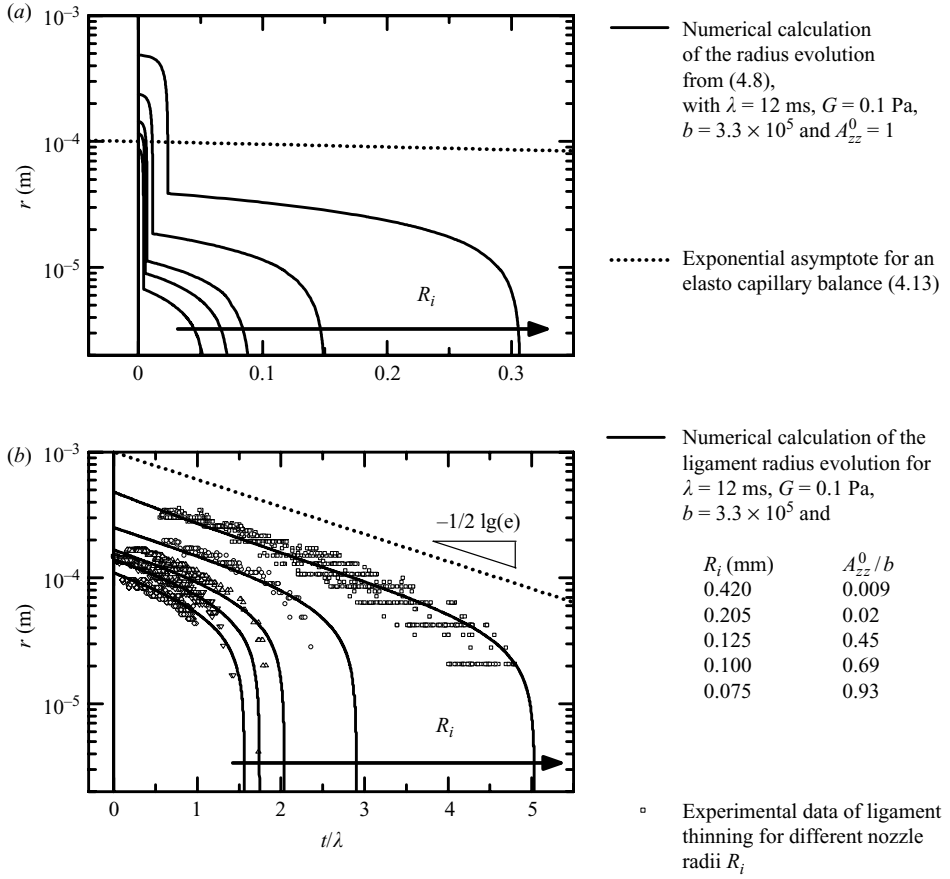
FIGURE 18. Numerical calculations of the thinning kinetics for the viscoelastic ligaments that interconnect the beads along the jet for nozzle inner radii of $R_i = 0.075, 0.1, 0.125, 0.205, 0.42$ mm. Predictions for $\lambda = 12$ ms, $b = 3.3 \times 10^5$, $G = 0.1$ Pa; and (a): $A_{zz}^0 = 1$, (b): $A_{zz}^0 = 3 \times 10^3$ (for $R_i = 0.42$ mm) to $A_{zz}^0 = 3.1 \times 10^5$ (for $R_i = 0.075$ mm). The broken line shows the prediction of the asymptotic theory for the elastocapillary quasi-equilibrium regime. The open symbols are experimentally observed ligament radii.

($r = 0$). The results for t_{br} obtained from figure 18(a) are presented in figure 11 as the dotted line. While these results do show the systematic dependence of the breakup time on the nozzle radius also observed in experiments, the predicted breakup times are an order of magnitude below the experimental observations. Furthermore, the numerical calculations in figure 18(a) show a pronounced first stage of inertiocapillary thinning (§4.3) with a fast initial drop in filament radius over an order of magnitude, which is not observed in the experimental images of figures 1 or 3. The reasons for this are manifold; from inadequacy of the estimates for molecular parameters to the very simple dumbbell model selected to describe the polymer chains. Nonetheless, the FENE model correctly describes the results obtained in capillary breakup extensional rheometry (§2.1). A comparison of the observed diameter evolution in the CaBER device after a step strain with the predictions of the FENE model in figure 2 leads to a realistic estimate of the modulus $G = 0.1$ Pa and finite extensibility $b = 3.3 \times 10^5$ as suggested by molecular estimates, and the theory matches the experiment in figure 2

rather well. The source of discrepancy between experiments and theory in the constant-force thinning of a thin jet must therefore lie elsewhere.

One option that is certainly worth further examination is related to the 'initial' state of polymer molecules in the fully developed jet exiting the nozzle. It is quite plausible that the polymer molecules are partially oriented and elongated after exiting the syringe nozzle. Fluid elements at the exit undergo a small local die swell (leading to $R_0 > R_i$) and the velocity field in the jet must rapidly rearrange to develop a plug flow profile (Apelian, Armstrong & Brown 1988) resulting in potentially large non-zero initial elastic stresses in the jet. The short residence time of fluid elements in the present experiments (compared to the fluid relaxation time) gives an intrinsic Deborah number $De_0 = \lambda/\tau_R = 12/1 \gg 1$ (McKinley 2005). This also indicates that any effects of this initial configuration can propagate substantially along the jet as the growing fluid column begins to exhibit the Rayleigh plateau instability described in §4.3. Numerical calculations of drop ejection with a FENE dumbbell model (Yarlanki & Harlen 2008) show that this rearrangement in the velocity field near the stick-slip singularity at the nozzle exit coupled with the high shear rates near the wall of the needle can indeed cause significant molecular elongation. Such simulations also show that this preorientation is radially inhomogeneous with a thin sheath of prestretched material surrounding a relaxed core of unstretched material. Of course, a radially averaged theory of the type presented in §§4.2–4.4 will not be able to capture this radial elastic boundary layer and quantitative comparison with our experiments must await advances in time-dependent free-surface viscoelastic simulation. However, to demonstrate the importance of this prestretch we consider a simplistic case in which we generate a uniform average level of axial prestretch A_{zz}^0 in the polymer molecules entering the jet. In the model equations above, we thus should use $A_{zz}^0 > 1$; $A_{rr}^0 = A_{zz}^{0\,-1/2}$ and we also have to incorporate this contribution of the initial extension into the upstream value of the axial force in the jet in (4.2):

$$F = \pi \gamma R_0 + G \pi R_0^2 \left(A_{zz}^0 - A_{zz}^{0\,-\frac{1}{2}} \right).$$

Repeating the numerical calculations for the evolution of the ligaments between beads in the jet, we can determine the value of the prestrain A_{zz}^0 that gives a reasonable fit to the experimental observations of breakup times. The results are shown in figure 18(b) for a prestretch ranging from $A_{zz}^0 = 3 \times 10^3$ for the larger nozzle radii to $A_{zz}^0 = 3.1 \times 10^5$ for the smallest nozzle ($A_{zz}^0/b = 0.009 - 0.93$). For comparison, also experimental measurements of the thinning ligament radius determined from sequences of video images for the specific case of gobbling close to critical conditions are shown in figure 18(b) and these are in accord with the numerical data. The prestretch introduced in the numerical calculations of figure 18(b) prevents the occurrence of a first stage of inertiocapillary thinning that was observed in figure 18(a). Furthermore, the required prestretch values lead, for smaller nozzle radii, to initial ratios $A_{zz}^0/b > 0.1$, the value that marks the onset of finite extensibility effects and the third stage type thinning described in §4.5. For very small nozzle radii, this stretch is continuously increasing over the course of the numerical calculations and prohibits the establishment of the second stage of elastocapillary thinning given by (4.13). Finite extensibility effects play a role right from the beginning when the jet exits the nozzle, again in reasonable agreement with the experimental observations in figure 18(b).

The good agreement between the experimental measurements of the ligament thinning kinetics and the numerical calculation in the elastocapillary and finite

extensibility regimes further support the necessity of incorporating the prestretch in order to describe quantitatively the evolution of the elastic ligaments during gobbling. For completeness the breakup times obtained from the numerical calculations including the prestretch are also shown in figure 11 (dashed line) and are close to the apparent breakup times. Further improvements in this simple constant-force thinning theory require a more realistic description of macromolecular behaviour during rapid elongation. However, even the simplified dumbbell model we have used provides quite satisfactory predictions of the general trends observed in the breakup times.

5. Conclusion

The 'gobbling' phenomenon observed at the transition from dripping to jetting for thin jets of dilute polymer solutions is essentially a form of delayed dripping: the result of the dynamic interaction of capillary breakup in a falling viscoelastic jet with a large terminal drop that serves as a sink for the mass and momentum of the incoming fluid. In the 'true gobbling' regime the jet breakup proceeds independently of the terminal drop motion; the polymeric additive primarily controls the longevity of the slender fluid filaments that form between beads in the latter stages of jet breakup. The presence of a finite relaxation time regularizes the complex dynamics observed in dripping-jetting transitions of Newtonian and generalized Newtonian fluids (Coullet *et al.* 2005; Yildirim & Basaran 2006). The viscoelastic filaments do support a significant tensile force which is transferred to the terminal drop and thus controls its dynamics. Our momentum balances show that this force can be estimated as the capillary force present in the upstream segment of the jet. The gobbling behaviour can be predicted quantitatively by a theory combining elementary mass and momentum balances for the jet and for the terminal drop in conjunction with theory for viscoelastic filament thinning and breakup that takes into account the existence of (constant) tensile forces in the ligaments between drops and finite extensibility of the polymeric molecules.

As a result of the persistence of the axial force, the breakup of these finite length fluid columns proceeds differently from the capillary breakup of an infinitely long liquid jet, which constitutes the foundation of the Rayleigh approach to jet breakup theory. The distinction is of minor concern for simple Newtonian fluids for which the breakup time is controlled by the early stage of capillary instability; however, it becomes crucial in the case of polymer solutions that are prone to substantial strain-hardening. It is anticipated that much of the previous work on viscoelastic jet breakup based on the Rayleigh approach should be revisited from this point of view. Since the transition is very sensitive to the viscoelastic characteristics of the polymer solutions, rheological properties of very dilute polymeric solution may be deduced from similar ' video-rheology' experiments.

Appendix A. Derivation of the parabolic trajectory of the terminal gobbling drop

We consider a short and rapidly flowing capillary jet between the nozzle and the terminal 'gobbling drop'. Although a convective capillary instability develops on the jet (figure 1), the jet appears stationary when considered on large time scales, with

high-frequency capillary perturbations superimposed on this time-averaged steady state. The mass balance and linear momentum balance for the terminal drop is given by (3.11) and (3.12). Using (3.11) and (3.7), the momentum balance (3.12) can be rewritten as

$$\rho \mathscr{V} \frac{\mathrm{d}U_d}{\mathrm{d}t} = \rho \frac{Q}{U_0} (U_0 - U_d)^2 + \rho \mathscr{V} g - \pi R_0 \gamma. \tag{A1}$$

Because Q, U_0 and R_0 are all time-independent, (3.11) and (A1) have simple first integrals. We can define the non-dimensional variables:

$$v = \frac{\mathscr{V}}{\mathscr{V}_0} \quad \text{and} \quad \tau = \frac{t}{t_0}, \quad \text{with} \quad \mathscr{V}_0 = \frac{F}{\rho g} \quad \text{and} \quad t_0 = \sqrt{\frac{\mathscr{V}_0 U_0}{g Q}} \equiv \sqrt{\frac{\gamma}{\rho g^2 R_0}}, \tag{A2}$$

where $\mathscr{V}_0$ compares the axial force to gravity and t_0 is the time scale on which the weight of the free falling jet balances the capillary force ($\rho g R_0^2 \cdot t_0^2 \sim \gamma R_0$). Then introducing (3.11) into (A1) we get

$$-\frac{\mathrm{d}}{\mathrm{d}\tau} (v \dot{v}) = v - 1, \tag{A3}$$

where $\dot{v} = \mathrm{d}v/\mathrm{d}\tau$. Substituting $\mu = v^2/2$ into (A3) results in

$$\frac{\mathrm{d}^2 \mu}{\mathrm{d}\tau^2} = -\sqrt{2\mu} + 1. \tag{A4}$$

This equation simply represents the motion of a material point of unit mass in a force field with the potential

$$\Phi(\mu) = \frac{2\sqrt{2}}{3} \mu^{3/2} - \mu. \tag{A5}$$

Therefore, the energy integral for this equation is

$$E = \tfrac{1}{2}\dot{\mu}^2 + \Phi(\mu) = \tfrac{1}{2}\dot{\mu}^2 + \tfrac{2}{3}\sqrt{2}\mu^{3/2} - \mu, \tag{A6}$$

or, using physical variables

$$E = \tfrac{1}{2}v^2 \dot{v}^2 + \tfrac{1}{3}m^3 - \tfrac{1}{2}v^2. \tag{A7}$$

If we use $\mu = v^2/2$ and $\nu = (\dot{v}^2 + 2v/3 - 1)$ as coordinates, then the level lines of the total energy E (which are trajectories corresponding to solutions of (A3)), are just hyperbolae in the μ, ν plane; the non-trivial trajectory corresponding to $E = 0$ is given by the equation

$$\dot{v} = \sqrt{1 - \tfrac{2}{3}v}. \tag{A8}$$

This equation can be solved explicitly for an initially zero drop volume (i.e. $v(0) = 0$) to give

$$\dot{v} = 1 - \tfrac{1}{3}\tau; \quad v = \tau - \tfrac{1}{6}\tau^2. \tag{A9}$$

In dimensional form we thus obtain an expression for the evolution in the volume of the terminal drop $\mathscr{V}(t)$:

$$\mathscr{V} = \pi R_0^2 \left(U^* t - \tfrac{1}{6} g t^2 \right); \quad U^* = \sqrt{\frac{\gamma}{\rho R_0}}, \tag{A10}$$

where the velocity scale U^* is the characteristic velocity of capillary waves on the jet of radius R_0 (Rayleigh 1879).
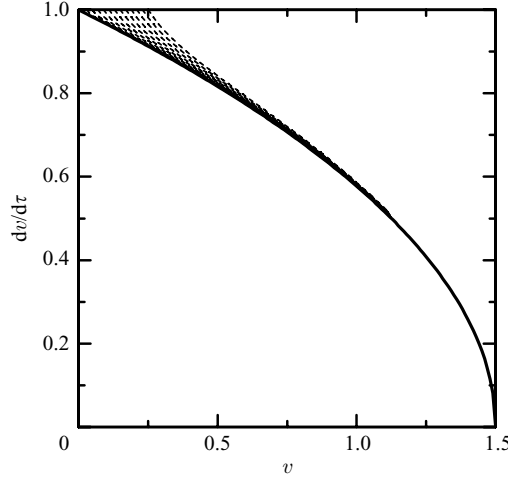
FIGURE 19. The rate of evolution of the volume of the terminal drop versus the scaled drop volume $v = \mathcal{V}/\mathcal{V}_0$; broken lines: trajectories corresponding to non-zero initial volume; solid line: the trajectory corresponding to negligible initial drop volume and expressed by (A 9).

Essentially, this analysis is (with minor modification due to the different prefactor in the force formulation) the solution derived by Clanet & Lasheras (1999) for the surface tension driven motion of a terminal drop at the end of a water column. The hyperbolic structure of the field level lines $\{\mu(t), v(t)\}$ shows that all trajectories eventually tend to this solution. This is confirmed by the direct numerical calculations presented in figure 19. Motion along the trajectories can also be described analytically by elliptic integrals.

This solution describes the slow dynamics of the evolution of the terminal drop volume; at a certain point, the drop suddenly detaches, and a new cycle starts. It is rather difficult, if not impossible, to adequately specify the initial conditions for the new cycle. However, this proves to be of minor concern, provided that the initial volume of the new terminal drop is small enough. It is obvious from figure 19, that all solutions starting with sufficiently small initial value of $v(t=0)$ are quickly attracted to the solid line expressed by the elementary solution (A 9) that corresponds to negligible initial volume. Therefore, this particular solution describes a robust feature of the 'gobbling' behaviour.

Rearranging (3.11), the velocity of the terminal drop can be expressed as:

$$U_d = \frac{\mathrm{d}L}{\mathrm{d}t} = U_0 \left(1 - \frac{\mathcal{V}_0}{t_0 Q} v \right).$$

Here, $L(t)$ is the current position of the terminal drop. As the above discussion has shown, one is justified in using the elementary solution (A 9) for $v(\tau)$ to describe the drop evolution in the gobbling regime. This results in the parabolic solution

$$U_d(t) = U_0 - U^* + \tfrac{1}{3}gt; \quad L(t) = L_{max} + \left(U_0 - U^* \right) t + \tfrac{1}{6}gt^2; \quad U^* = \sqrt{\frac{\gamma}{\rho R_0}}. \quad \text{(A 11)}$$

Appendix B. Dynamic theory for an accelerating jet

An obvious drawback of the elementary theory is that it does not take into account the variation in the fluid velocity along the jet caused by gravitational acceleration.

At flow rates close to critical conditions such variations become significant even for very thin jets. Indeed, the relative velocity variation can be estimated as

$$\frac{\delta U}{U_0} \sim \frac{g L_{max}}{U_0^2}.$$

This contribution ranges from 0.15 to 3.5 from our experiments and thus turns out to be important. In this Appendix the periodic jet theory presented previously is extended to the case of a fluid velocity $U(z)$ that varies along the jet. As in the previous case, we assume that the flow in the jet can be considered to be inviscid and the flow in the jet is quasi-steady on the time scale of 'gobbling'. Then the mass and momentum balances for a slender jet under steady state conditions become

$$\pi R^2 U = Q = const, \tag{B 1a}$$

$$\frac{\mathrm{d}}{\mathrm{d}z} \left(\rho \pi R^2 U^2 \right) = \rho g \pi R^2 + \frac{\mathrm{d}}{\mathrm{d}z} \left(\pi \gamma R \right). \tag{B 1b}$$

In (B 1b) the left-hand side is the linear momentum flux out of the control volume and the terms on the right-hand side are the contributions of gravity, and of the net axial force due to surface tension and pressure at any cross-section respectively. The z-axis is directed downwards; $R(z)$ and $U(z)$ are the local jet radius and velocity. Integrating (B 1) we find the velocity distribution along the length of the jet:

$$z = \frac{U^2}{2g} - \frac{U_0^2}{2g} + \frac{\gamma}{\rho g R_0} \left(\sqrt{\frac{U}{U_0}} - 1 \right), \quad R = R_0 \sqrt{\frac{U_0}{U}}, \tag{B 2}$$

R_0 and U_0 being the jet radius and velocity near the nozzle. Alternatively, in dimensionless variables (B 2) becomes

$$Bo \frac{z}{R_0} = \tfrac{1}{2} We \left(\frac{U^2}{U_0^2} - 1 \right) + \sqrt{\frac{U}{U_0}} - 1,$$

where $We = \rho U_0^2 R_0 / \gamma$ is the Weber number and $Bo = \rho g R_0^2 / \gamma$ the Bond number based on the initial jet radius.

For $Bo \ll 1$ the velocity profile $U(z)$ can be readily approximated by a quadratic function, and $R(z)$ is then evaluated using this approximate expression and (B 2). Notice that the velocity increases with distance from the nozzle, while the jet radius and therefore the net axial force decrease. Assuming that the jet radius and velocity are specified as functions of z, we can write the mass and momentum balances for the terminal drop as before in the form of (3.11). The only difference is that $U(z)$ and $F = \pi \gamma R(z)$ should now be evaluated at the current location $L(t)$ of the terminal drop using the jet profile determined by solving (B 2). This leads to the following set of differential equations:

$$\frac{\mathrm{d}L}{\mathrm{d}t} = U_d; \tag{B 3a}$$

$$\mathscr{V} \frac{\mathrm{d}U_d}{\mathrm{d}t} = \frac{Q}{U} (U - U_d)^2 + \mathscr{V} g - \frac{F}{\rho}; \tag{B 3b}$$

$$\frac{\mathrm{d}\mathscr{V}}{\mathrm{d}t} = Q \left(1 - \frac{U_d}{U} \right), \tag{B 3c}$$

with $U = U(L)$ and $F = \pi \gamma R(L)$. These equations can be integrated numerically. It is convenient to take initial conditions corresponding to the instant immediately after the terminal drop detachment, so that at $t = 0$, $\mathscr{V} = 0$ and $L = L_{max}$. Equations (B 3)
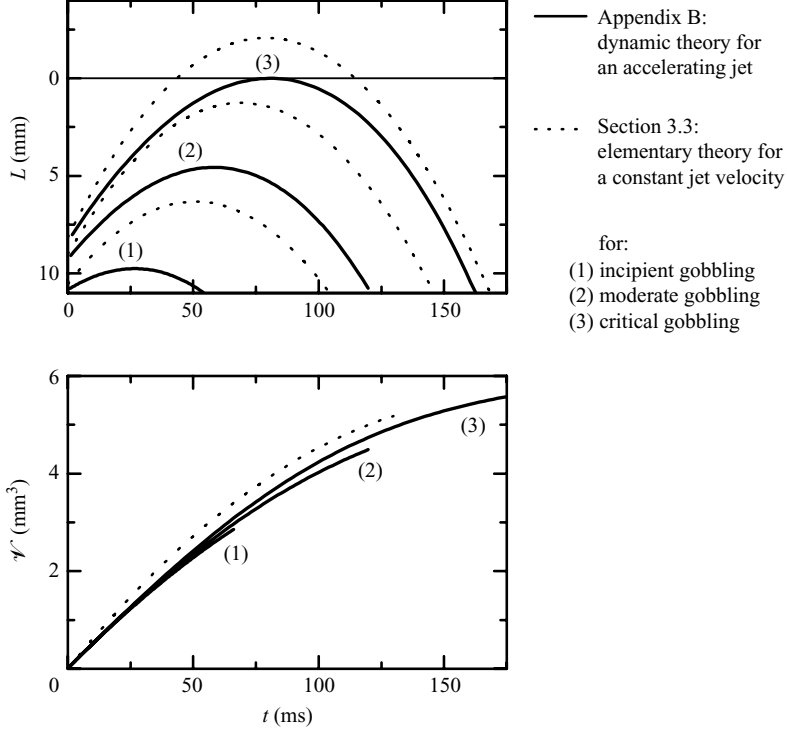
FIGURE 20. Oscillations of the terminal drop in a jet accelerating under gravity. Drop position and volume variation during an individual 'gobbling cycle' for a nozzle with an initial jet radius $R_0 = 0.188$ mm and a breakup time of $t_{br} = L_{max}/U_0 = 26$ ms. Solid lines: numerical solutions of the dynamic theory for an accelerating jet (B 3) for different values of $U_0 = 0.313, 0.35$ and 0.41 m s^{-1}. Dotted lines: analytical solutions of the elementary theory from equations (3.13) and (3.16) of §3.3.

require one more initial condition, the initial velocity U_d of the growing terminal drop. It is straightforward to check numerically that all solutions corresponding to different values of the initial velocity rapidly converge to a unique solution corresponding to the finite acceleration of a drop of initially vanishing volume that starts with a velocity:

$$U_d(t = 0) = U(L_{max}) - \sqrt{\frac{\gamma}{\rho R(L_{max})}}. \tag{B 4}$$

For a given initial jet radius R_0 and a specified maximum length L_{max}, solutions of (B 3) with the initial conditions stated above depend only on the flow rate Q (or equivalently the initial jet velocity U_0). An example is presented in figure 20. The profiles are evaluated for an initial jet radius $R_0 = 0.188$ mm and three different jet velocities $U_0 = 0.313, 0.35$ and 0.41 m s^{-1} that correspond to the three characteristic cases visualized in figure 3; (1) 'incipient gobbling' with vanishing oscillation amplitude, (2) 'moderate gobbling' with an amplitude equal to half of the critical length and (3) 'critical gobbling' with an amplitude equal to the maximum length of the jet. In these examples, the values for L_{max} are deduced from the breakup time measured experimentally for this particular jet radius: $L_{max} = U_0 t_{br}$ with $t_{br} = 26$ ms. Note that because of axial acceleration in the jet the actual time required for a fluid

particle exiting the nozzle to reach L_{max} is shorter than t_{br}. For instance the 'times of flight' corresponding to the three presented case are 22.9, 22.8 and 22.7 ms respectively.

We can finally compare these calculations to the results of the elementary theory of §3.3. The dynamic theory generally gives smaller oscillation amplitudes due to a smaller initial acceleration of the terminal drop. A direct comparison of experimental data for the position and mass of the end drop to the results of the elementary theory has been given in figure 9. The experimental data is well described by the dynamic theory of an accelerating jet.

REFERENCES

ADAMSON, A. W. & GAST, A. P. 1997 *Physical Chemistry of Surfaces*, 6th edn. Wiley-Interscience.

AMAROUCHENE, Y., BONN, D., MEUNIER, J. & KELLAY, H. 2001 Inhibition of the finite-time singularity during droplet fission of a polymeric fluid. *Phys. Rev. Lett.* **86** (16), 3558–3561.

AMBRAVANESWARAN, B., SUBRAMANI, H. J., PHILLIPS, S. D. & BASARAN, O. A. 2004 Dripping-jetting transitions in a dripping faucet. *Phys. Rev. Lett.* **93** (3), 034501.

ANNA, S. L. & MCKINLEY, G. H. 2001 Elasto-capillary thinning and breakup of model elastic liquids. *J. Rheol.* **45** (1), 115–138.

APELIAN, M. R., ARMSTRONG, R. C. & BROWN, R. A. 1988 Impact of the constitutive equation and singularity on the calculation of stick slip-flow – the modified upper-convected maxwell model (mucm). *J. Non-Newton. Fluid Mech.* **27** (3), 299–321.

BAZILEVSKII, A. V., ENTOV, V. M. & ROZHKOV, A. N. 1990a Liquid filament microrheometer and some of its applications. In *Third European Rheology Conference* (ed. D. R. Oliver), pp. 41–43. Elsevier Applied Science.

BAZILEVSKII, A. V., ENTOV, V. M. & ROZHKOV, A. N. 2001 Breakup of an oldroyd liquid bridge as a method for testing the rheological properties of polymer solutions. *Vysokomol. Soedin. Ser. A* **43** (7), 716–726.

BAZILEVSKII, A. V., ENTOV, V. M., ROZHKOV, A. N. & YARIN, A. L. 1990b Polymeric jets, beads-on-string breakup and related phenomena. In *Third European Rheology Conference* (ed. D. R. Oliver), pp. 44–46. Elsevier Applied Science.

BIRD, R. B., ARMSTRONG, R. C. & HASSAGER, O. 1987 *Dynamics of Polymeric Liquids. Volume 1: Fluid Mechanics*, 2nd edn. Wiley Interscience.

BOUSFIELD, D. W., KEUNINGS, R., MARRUCCI, G. & DENN, M. M. 1986 Nonlinear-analysis of the surface-tension driven breakup of viscoelastic filaments. *J. Non-Newton. Fluid Mech.* **21** (1), 79–97.

BOYS, C. V. 1958 *Soap Bubbles: Their Colors and Forces Which Mold Them*, Dover Publications.

BRAITHWAITE, G. J. C. & SPIEGELBERG, S. H. 2001 A technique for characterizing complex polymer solutions in extensional flows. In *Society of Rheology 72nd Meeting*, EF2.

CHRISTANTI, Y. & WALKER, L. M. 2001 Surface tension driven jet break up of strain-hardening polymer solutions. *J. Non-Newton. Fluid Mech.* **100** (1–3), 9–26.

CLANET, C. & LASHERAS, J. C. 1999 Transition from dripping to jetting. *J. Fluid Mech.* **383**, 307–326.

CLASEN, C., BICO, J., ENTOV, V. M. & MCKINELY, G. H. 2004 Video-rheology – studying the dripping, jetting, breaking, and "gobbling" of polymeric liquid threads. In *The XIVth International Congress on Rheology* (ed. J. W. Lee & S. J. Lee), vol. RE33, pp. 1–3. The Korean Society of Rheology.

CLASEN, C., EGGERS, J., FONTELOS, M. A., LI, J. & MCKINLEY, G. H. 2006a The beads-on-string structure of viscoelastic threads. *J. Fluid Mech.* **556**, 283–308.

CLASEN, C., PLOG, J. P., KULICKE, W. M., OWENS, M., MACOSKO, C., SCRIVEN, L. E., VERANI, M. & MCKINLEY, G. H. 2006b How dilute are dilute solutions in extensional flows? *J. Rheol.* **50** (6), 849–881.

COULLET, P., MAHADEVAN, L. & RIERA, C. S. 2005 Hydrodynamical models for the chaotic dripping faucet. *J. Fluid Mech.* **526**, 1–17.

CRASTER, R. V., MATAR, O. K. & PAPAGEORGIOU, D. T. 2005 On compound liquid threads with large viscosity contrasts. *J. Fluid Mech.* **533**, 95–124.

EGGERS, J. 1997 Nonlinear dynamics and breakup of free-surface flows. *Rev. Mod. Phy.* **69** (3), 865–929.

ENTOV, V. M. & HINCH, E. J. 1997 Effect of a spectrum of relaxation times on the capillary thinning of a filament of elastic liquid. *J. Non-Newton. Fluid Mech.* **72** (1), 31–53.

ENTOV, V. M. & YARIN, A. L. 1984 Influence of elastic stresses on the capillary breakup of jets of dilute polymer solutions. *Fluid Dyn.* **19** (1), 21–29.

GOLDIN, M., YERUSHALMI, J., PFEFFER, R. & SHINNAR, R. 1969 Breakup of a laminar capillary jet of a viscoelastic fluid. *J. Fluid Mech.* **38** (4), 689–711.

GRIFFITH, A. A. 1926 The phenomena of rupture and flow in solids. *Phil. Trans. R. Soc. Lond. Ser. A* **221**, 163–198.

HARKINS, W. D. & BROWN, F. E. 1919 The determination of surface tension and the weight of falling drops. *J. Am. Chem. Soc.* **41**, 499–524.

KLIAKHANDLER, I. L., DAVIS, S. H. & BANKOFF, S. G. 2001 Viscous beads on vertical fibre. *J. Fluid Mech.* **429**, 381–390.

MCKINLEY, G. H. 2005 Visco-elasto-capillary thinning and breakup of complex fluids. In *Annu. Rheol. Rev.* (ed. D. M. Binding & K. Walters), vol. 3, pp. 1–48. British Society of Rheology.

MCKINLEY, G. H. & SRIDHAR, T. 2002 Filament-stretching rheometry of complex fluids. *Annu. Rev. Fluid Mech.* **34**, 375–415.

MCKINLEY, G. H. & TRIPATHI, A. 2000 How to extract the Newtonian viscosity from capillary breakup measurements in a filament rheometer. *J. Rheol.* **44** (3), 653–670.

MIDDLEMAN, S. 1965 Stability of a viscoelastic jet. *Chem. Engng Sci.* **20**, 1037–1040.

PEARSON, J. R. 1985 *Mechanics of Polymer Processing*. Springer.

PLOG, J. P., KULICKE, W. M. & CLASEN, C. 2005 Influence of the molar mass distribution on the elongational behaviour of polymer solutions in capillary breakup. *Appl. Rheol.* **15** (1), 28–37.

RAYLEIGH, LORD 1879 On the capillary phenomena of jets. *Proc. R. Soc. Lond. Ser. A* **29**, 71–79.

RAYLEIGH, LORD 1892 On the instability of a cylinder of viscous liquid under capillary forces. *Phil. Mag.* **34** (207), 145–154.

RIBE, N. M., HUPPERT, H. E., HALLWORTH, M. A., HABIBI, M. & BONN, D. 2006 Multiple coexisting states of liquid rope coiling. *J. Fluid Mech.* **555**, 275–297.

ROZHKOV, A. N. 1983 Dynamics of threads of diluted polymer solutions. *J. Engng Phys. Thermophys.* **45** (1), 768–774.

SATTLER, R., WAGNER, C. & EGGERS, J. 2008 Blistering pattern and formation of nanofibers in capillary thinning of polymer solutions. *Phys. Rev. Lett.* **100** (16), 164502.

SAUTER, U. S. & BUGGISCH, H. W. 2005 Stability of initially slow viscous jets driven by gravity. *J. Fluid Mech.* **533**, 237–257.

TIRTAATMADJA, V., MCKINLEY, G. H. & COOPER-WHITE, J. J. 2006 Drop formation and breakup of low viscosity elastic fluids: effects of molecular weight and concentration. *Phys. Fluids* **18** (4), 043101.

WAGNER, C., AMAROUCHENE, Y., BONN, D. & EGGERS, J. 2005 Droplet detachment and satellite bead formation in viscoelastic fluids. *Phys. Rev. Lett.* **95** (16), 4.

WEBER, C. 1931 Zum Zerfall eines Flüssigkeitsstrahls. *Z. Angew. Math. Mech.* **11** (2), 136–154.

YARLANKI, S. & HARLEN, O. G. 2008 Jet breakup of polymeric liquids. In *XXII International Congress of Theoretical and Applied Mechanics*. Adeleide, Australia.

YILDIRIM, O. E. & BASARAN, O. A. 2006 Dynamics of formation and dripping of drops of deformation-rate-thinning and -thickening liquids from capillary tubes. *J. Non-Newton. Fluid Mech.* **136** (1), 17–37.